Effects of Oxide film, Fe-rich phase, Porosity and their Interactions on Tensile Properties of Cast Al-Si-Mg Alloys

Kittiphan Bangyikhan

A thesis submitted to the Faculty of Engineering of
The University of Birmingham
for the degree of
Doctor of Philosophy

School of Metallurgy and Materials
Faculty of Engineering
University of Birmingham
Birmingham B15 2TT
United Kingdom

June 2005

Pages 0 to 74
Title page, introductory matter, Chapters 1 - 3

Chapters 4 to 7 and references are in 2 additional files

ABSTRACTS

Since mechanical properties of cast Al-Si-Mg alloys are directly influenced by microstructural defects, understanding the characteristics of these defects and any interactions between them is important for improving the properties of castings. This research studied the effect of the most common defects normally found in cast aluminium alloys namely, double oxide films, Fe-rich phase, and porosity. A different level of each defect was introduced into the castings to investigate their effects on tensile properties with the results analysed by Yate's algorithm and Weibull statistical analysis to determine their relative effects. The most important defect in this research was the oxide film that had an effect on UTS and elongation of about 21 MPa and 0.9% respectively and on the UTS Weibull modulus and elongation Weibull modulus of about 37 and 3 respectively. Increasing Fe content from 0.1 to 0.5 wt% influenced the tensile properties of the castings by decreasing the UTS and elongation by about 28 MPa and 1.7 % respectively. Although Fe-rich phases produced the greatest effect on tensile properties, their relatively high Weibull modulus showed that the reliability of the castings was at least predictable compared to the effects associated with oxide films. The porosity defects caused by an increase in hydrogen content from 0.1 to 0.45 ml/100g metal were the least detrimental to tensile properties.

The most important interaction found in this research was the interaction between oxide films and porosity suggesting a mechanism for porosity formation in which entrained oxide film acted as initiation sites for pore formation in the castings. The main factor in the formation of porosity was hydrogen and shrinkage, since both could encourage the expansion of the oxide film defects to become gas porosity or shrinkage porosity in the castings. The other interaction between the microstructural defects observed in this research was that oxide films were found to be substrates for the nucleation and growth of Fe-rich phases, particularly the β-Al_5FeSi phase. An interaction between all three defects were also observed and it further influenced the tensile properties of the cast Al-Si-Mg alloys by decreasing UTS and elongation by about 5 MPa and 0.5% respectively and the UTS Weibull modulus and elongation Weibull modulus of about 8 and 0.6 respectively.

ACKNOWLEDGEMENTS

During working on this thesis many people have helped me and I would like to acknowledge to the following.

I would like to give special thanks to my supervisor Dr. W. D. Griffiths for all of his advice, guidance, and encouragement, without which this work would never have been completed. It has been my pleasure to work with him.

My sincere acknowledgements are due to the Department of Primary Industries and Mines, Ministry of Industry (Thailand), and the University of Birmingham (United Kingdom) for the financial assistance of the program.

I would like to thank Adrain Caden, Mick Wickens, Dave Price, Jaz Singh, Lesley Tomkins and other technical staff at the school of Metallurgy and Materials for their help and assistance. I would never have been able to carry out the experimental work without them.

I would like to acknowledge the people who helped with the computer modelling at the Interdisciplinary Research Centre in Materials Processing, including Masood Turan and Jean-Christophe Gebelin. I would also like to thank Peter Thornton and Bill Hewitt at the school of Mechanical and Manufacturing Engineering for their help on machining techniques.

I would like to thank Prof. John Campbell and my colleagues, Derya Dispinar, Nan-Wei Lai, Ramin Raiszadeh, Pual Davies and past members of the casting group for their help and many useful discussions.

Finally, I would like to thank my mother, Boonmee Bangyikhan, and my family for their love and support and Natcha Thampidoksutti for her support throughout the final year of this thesis.

CONTENTS

CHAPTER 1

INTRODUCTION

Cast Al-Si-Mg alloys have excellent combinations of properties, for example, high strength-to-weight ratio, good fluidity, and good corrosion resistance. These alloys, therefore, find widespread applications in general engineering and meet the increasing demands of the automotive and aerospace industries.

Nevertheless, the benefits of Al-Si-Mg alloys have been restricted since the mechanical properties attainable in this alloy are influenced by several microstructural defects. Many researches have shown that, among many defects occurring during the casting process, the microstructural defects that have significant effects on mechanical properties are Fe-rich intermetallic phases, porosity, and oxide films. Iron is well known as an undesirable impurity in aluminium alloys and forms an intermetallic phase in the casting. The morphology of Fe-rich phases, particularly β-Al_5FeSi phase, which is the platelet- or needle-like phase, plays an important role in reducing mechanical properties of the castings. Porosity occurs during solidification by two primary causes, the evolution of hydrogen and the inadequate feeding of the volume contraction during the phase change. This kind of defect can be detrimental to mechanical properties of castings due to a decrease in the load bearing area. Finally, oxide films or double oxide film defects, caused by the entrainment of the surface oxide of the melt during casting and which is carried into the final microstructure, play a major role in the control of properties since they act as cracks inside the casting. It has been reported that the reliability and reproducibility of cast aluminium alloys is also influenced by oxide film defects due to the variety of shape and sizes. In addition, the difficulty of measurement of oxide film defects with any non-destructive testing methods has hindered understanding of how the defects may be removed.

Besides their individual effects on mechanical properties produced by these defects, their interrelationships have been suggested by many authors. A number of researches have

reported several interesting interactions between them, for example, the presence of porosity defects in association with oxide films and Fe-rich phases. It has been suggested that nucleation of pores in cast aluminium alloys is unlikely to occur in practice in the case of both homogeneous and heterogeneous nucleation due to the extremely high pressure required. Oxide films and Fe-rich phases therefore might lead to the formation of pores in the castings. Several authors also suggested another interaction between the microstructural defects, that the oxide films acted as nucleation sites for Fe-rich phases. However, there has been no work to date that clearly describes the interrelationships between these defects.

Many techniques have been developed over the years to minimise the number of defects in a casting, including gas content control, melt temperature control, microstructural control by chemical addition and/or cooling rate, and improvements in mould design. However, defects are still unavoidable in castings and limit the use of cast aluminium alloys. Therefore it is important to understand the characteristics of these defects, their formation mechanisms, and the interactions between them in order to obtain more efficient use of the castings.

The aim of the present research, therefore, is to investigate the effects of oxide film, Fe-rich phase, and porosity defects, (both hydrogen gas porosity and shrinkage porosity), with respect to tensile properties in a cast Al-Si-Mg alloy. The formation of these defects and their association with each other is also commented upon. The main purpose of the study is to investigate whether 1) intermetallic compounds, particularly β-Al_5FeSi phases, nucleate on oxide films, 2) the formation of porosity is associated with oxide films and Fe-rich phases, 3) porosity is associated with Fe-rich phases, and 4) whether all three defects introduce any interrelationship.

CHAPTER 2

LITERATURE REVIEW

Cast Al-Si-Mg alloys, containing normally 7 wt% Si and about 0.25 to 0.7 wt% Mg, have widespread applications especially in the aerospace and automotive industries. These foundry alloys possess excellent tensile properties and good corrosion resistance. The addition of silicon imparts excellent castability and resistance to hot-tearing in these alloys. Also, since silicon leads to an increase in volume during solidification, the susceptibility of the castings to shrinkage defects is reduced. Consequently, aluminium alloys containing silicon are ideally suited for high volume production in the aluminium foundry [Sigworth et al. 1989]. Magnesium is often added in automotive versions of the alloy for strengthening and hardening purposes. Magnesium contents are typically less than about 0.7% because increased additions impair fluidity and feeding [Narayanan et al. 1994, Samuel et al. 1998].

In general, the mechanical properties are controlled by the microstructural constituents that precipitate upon solidification, depending upon the composition and solidification conditions of the alloy [Samuel and Samuel 1992]. Also, the mechanical properties of castings are strongly influenced by impurities and undesirable microstructural features [Ravi et al. 2002]. To improve casting quality and produce reliable castings, several techniques have been developed, and can be categorise as 1) control of the liquid metal prior to casting, 2) control of the pouring of liquid metal into the mould and any metal/mould reaction, and 3) control of casting microstructure and defects during solidification. However, recent research has suggested that cast aluminium alloys are, at best, only achieving and using one per cent of their potential mechanical properties, particularly in terms of fatigue life, due to the presence of microstructural defects in the castings [Cao and Campbell 2003]. A number of researchers have shown that the most detrimental microstructural defects that are usually found in Al-Si-Mg alloy castings are oxide films (a non-metallic inclusion), porosity, and Fe-rich intermetallic phase

[Backerud et al. 1990, Crepeau 1995, Samuel and Samuel 1992, Singh and Mitchell 2001, Campbell 2003, Dai et al, 2003].

2.1 Oxide film defects in cast Al-Si-Mg alloys

The term 'inclusion' refers to undissolved foreign material present in a cast metal [Kaye and Street 1982]. Inclusions are well known as a common feature of the alloy composition that are normally introduced into the castings during the production process. They can broadly be classified as solid inclusions, liquid inclusions (e.g., cryolite coming from the alumina electrolyte), and fluxes that are suspended in the melt as a result of previous fluxing treatments [Apelian 1998]. One of the most detrimental defects found in cast aluminium alloys are non-metallic inclusions as they act as stress-raisers and cause failure of castings [Makarov et al. 1999, Singh and Mitchell 2001]. Inclusions do not only impair mechanical properties, but also adversely affect machinability, porosity and corrosion resistance. Inclusions found in the casting vary by type and particle sizes range from a few microns to several millimetres. Typical inclusions that may be present in cast aluminium alloys are given in Table 2.1 [Makarov et al. 1999].

Among the inclusions in aluminium alloys, oxides are the most frequently found because of the strong affinity of aluminium for oxygen. Aluminium oxides observed in the casting can form in different types, ranging in specific gravity from 2.3 to 4, depending upon oxidation temperature, time and thickness [Davis 1993, Jeurgens et al. 2002]. Oxide inclusions can appear at the beginning of melting since they arrive as oxide skins on the surface of the charged material. When remelted in a furnace, its surface oxides therefore become suspended in the melt. Also oxide inclusions can be present in the casting if they were formed during preparation of the melt, transfer, or mould filling. Finally oxides are found as massive, film-like, or dross-like inclusions in finished castings [Campbell 2003].

Table 2.1 Classification of inclusions observed in molten aluminium [Makarov et al., 1999].

Type	Form	Density (ρ_p g/cm^3)	Dimensions (μm)	MP (^{o}C)
Oxides				
$MgAl_2O_4$ (spinel)	Particles, skins, flakes	3.60	0.1-100, 10-5000	2825
Al_2O_3 (corundum)	Particles, skins	3.97	0.2-30, 10-5000	2047
MgO	Particles, skins	3.58	0.1-5, 10-5000	2115
SiO_2	Particles	2.66	0.5-30	1650
CaO	Particles	3.37	<5	2630
Carbides				
Al_4C_3	Particles, clusters	2.36	0.5-25	2100
SiC	Particles	3.22	0.5-5	2540
Borides				
TiB_2	Particles, clusters	4.5	1-30	2790
AlB_2	Particles	3.19	0.1-3	2160
Nitrides				
AlN	Particles, skins	3.26	10-50	2227
Other				
Chlorides and salts ($CaCl_2$, NaCl, $MgCl_2$)	Liquid droplets	1.9-2.2	0.5-1	712-800
Fluorides (cryolite)	-	2.9-3.0	-	1000
Sludge Al(FeMnCr)Si	-	>4.0	-	-
Ultrafine gas bubbles	-	-	10-30	-
Argon bubbles N_2 bubbles	Particles, clusters	-	10-100	-
Intermetallics ($TiAl_3$, TiAl, ,NiAl, Ni_3Al)				

2.1.1 Formation of oxide films

Oxide films are formed on the surface of liquid metal when it is exposed to an atmosphere containing oxygen [Sleppy 1961, Silva and Talbot 1988, Impey et al. 1988, Jeurgens et al. 2002]. In pure aluminium, the initial oxide film formed on the molten aluminium surface is an amorphous form of Al_2O_3 due to the randomly distributed atoms of liquid metal. This amorphous oxide film is impermeable to diffusion of aluminium metal and oxygen because of the lower mobility of charge carriers in amorphous

materials. This film, therefore, forms a protective layer over the molten aluminium [Silva and Talbot 1988]. A further factor limiting the mobility of the diffusing species in an amorphous material is the absence of preferred diffusion paths such as grain boundaries. The amorphous film is unstable compared to the crystalline counterpart and will transform by nucleation and growth of a crystalline form if given time and opportunity [Silva and Talbot 1988].

After an incubation time of 5-10 minutes at 750 ^{o}C, the amorphous film may develop to a crystalline form of γ-Al_2O_3 or η-Al_2O_3 film [Haginoya and Fukusako 1983, Impey et al. 1991]. The transformation of amorphous to crystalline alumina nucleates and grows rapidly at the melt/oxide surface [Dignam 1962, Impey et al. 1991]. Werfers and Misra [1987] assumed that the crystalline alumina grew laterally and vertically by the further continuous oxidation of metal, not by recrystallization of the amorphous film. Therefore, oxygen must be supplied from the atmosphere. At a temperature of around 700 ^{o}C, the rate of lattice diffusion in refractory oxides such as Al_2O_3 is too slow to provide enough oxygen, therefore, open pathways between the atmosphere and the melt are required to maintain the reaction between aluminium and oxygen. Agema and Fray [1989] proposed that oxidation resulted from the transportation of matter (oxygen) through the continuous pathways which penetrated the oxide film. The pathways in the oxide films at the surface of the melt could be cracks, pores, or zones of loose structure inherent in the films, or formed by the volume change associated with conversion of metal to oxide. Another mode proposed by Sleppy [1961] was oxidation achieved by the diffusion of aluminium ions through the oxide film. However, the difficulty for this model was that the oxide was almost impermeable to the diffusion of both metal and oxygen. Campbell [2000] suggested that fresh supplies of metal arrive at the surface of the film not by diffusion, which is slow, but by flow of the melt along capillary channels, which is, of course, much faster.

It was reported that, after crystalline γ-Al_2O_3 or η-Al_2O_3 film were formed, they would be subject to further transformation to α-Al_2O_3 crystal or corundum with time and at temperature. Wilson and Connell [1980] suggested that the transformation from γ-Al_2O_3 to α-Al_2O_3 was difficult to bring about in the practice since total conversion occurred on

heating above 1200 ^{o}C for more than one hour. The crystallization of α-Al_2O_3, however, has been reported to be achieved at a temperature of 750 ^{o}C after an incubation time of about 5 hours in industrial grade 319 alloy (Al-6Si-3Cu alloy) [Impey et al. 1988]. Traces of α-Al_2O_3 have been identified even at early stages of melting. This transformation results in a 24% reduction in oxide volume and is thought to cause film rupture further exposing the liquid metal beneath to oxidation. Therefore the development and growth of oxide films on liquid Al alloys results from local penetration of the thin, first-formed oxide film by liquid metal which has exuded through the film. The melt then will contact the atmosphere where it reacts with oxygen to form alumina on the existing Al_2O_3 film [Impey et al. 1991].

When aluminium alloys contain magnesium, the oxidizing tendency of the molten metal increases rapidly with magnesium content. The melt oxidation is expected to form pure MgO or magnesia when the magnesium content of the alloy is raised to above 2 wt % in aluminium, since MgO has a lower free energy of formation than Al_2O_3 [Makarov 1999]. At intermediate magnesium levels of between 0.005 and 2 wt % a mixed oxide $MgO.Al_2O_3$, known as spinel, is formed [Campbell 2000]. Depending on the magnesium content in aluminium alloys the oxidation reaction path possibly starts with the formation of amorphous MgO, or $MgAl_2O_4$, or Al_2O_3, that then transforms to crystalline MgO, or $MgAl_2O_4$, or γ-Al_2O_3 film. With the progressive depletion of magnesium at the oxide-melt interface the oxide films change from magnesia, to spinel and finally to alumina. As a result of the volume change, the oxide film is subject to the build up of considerable local stress and is, therefore, inclined to deform or crack. Liquid metal may exude to the surface through the crack which will, of course, develop a new oxide envelope. When the magnesium concentration at the melt-oxide interface falls to below a critical level, localised nucleation and formation of $MgAl_2O_4$ is favoured by preferential breakaway oxidation.

The nucleation and growth of oxide films is controlled by many factors, for example, temperature, alloying elements, and ambient humidity. Temperature was reported to be the most important factor since it accelerated the oxidation of molten aluminium [Sleppy 1961]. Different alloying elements have different effects on the strengths and the

oxidation reaction rates of oxide films, depending on their contribution to the density of the oxide film layer, or their influence on the mobility of ionic transport in the oxide [Thiele 1962]. Cu, Fe, Si, Mn have a minimal effect on the oxidation of molten aluminium, whereas Mg, Na, Se, and Ca enhance the rate of oxidation [Thiele 1962, Agema 1989]. It was found that the strength of the oxide film increased with an increase of temperature and time. Also, Mg, Na, Se, and Ca had increased the strength of their oxide films whereas additions of Be, Si, Ta, and Sr decreased its strength [Agema 1989].

2.1.2 Morphology of oxide films

Oxide films exhibit a variety of appearances because of their different chemical compositions, thickness, strength and interaction with the melts. Figure 2.1 shows an example of oxide film observed on the fracture surface of a cast Al-5Mg alloy. Campbell [2000] described the morphology of oxide films as young and old oxide films to differentiate the behaviour of the oxide film according to their different thickness. The thickening of the oxide film was early observed by Thiele [1962] who reported that, after 5 seconds at 700 ^{o}C, the measured oxide film thickness on the surface of a melt was 24 nm and it increased to 900 nm when the melt was held for 1 hour at the same temperature. Campbell [2000] estimated the rate of thickening of the oxide film in aluminium alloy holding furnaces by measuring the weight of oxide film on surface of melt and showed that the growth of oxide film was approximately $7x10^{-7}$ $(kg/m^2)/s$, which was an order of magnitude faster than rates of growth of protective films on solid metals.

Thickness measurements are broadly divided into two methods. The first method employs scanning electron microscopy to image the film. By estimating the width of the smallest wrinkle or crease, *w*, the thickness of the film can be approximated to be *w*/2 (see Figure 2.1). This method may be accurate only for sharp folds that contain little or no trapped metal. Alternatively in some cases, an edge-on view of an oxide film will reveal the thickness of the film directly. In the second method, the oxide layer of a molten alloy is scraped away and the interference colours that form over time noted.

Using the corresponding wavelengths of light and correcting for reflected radiation the oxide thickness can be calculated [Agema 1989].

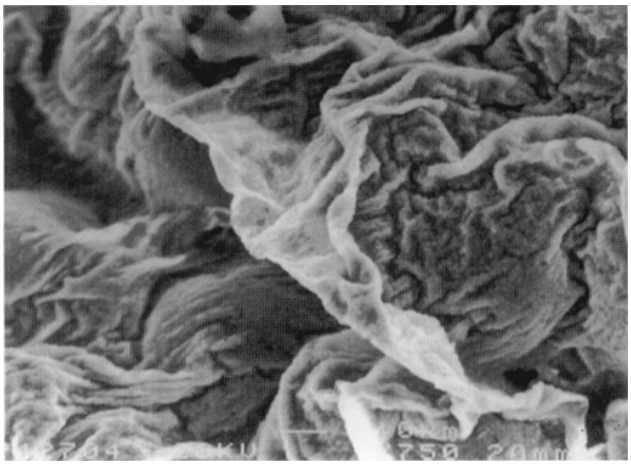

Figure 2.1 The SEM image showing the wrinkled nature of oxide film defect observed on the fracture surface of a cast Al-5Mg alloy [Campbell 2003]

Young films are characterized by their very thin thickness, some hundreds of nanometres thick. The fine wrinkled nature of young oxide films is related to the dynamics of the liquid metal immediately after their formation. Therefore, young oxide films are formed during pouring or mould filling since this process normally takes several seconds to tens of seconds [Campbell 2000]. Given time, young oxide films will thicken and turn into old oxide films (see Table 2.2). The necessary conditions are further reactants i.e., oxygen, aluminium or magnesium, and sufficient temperature. The thickness of old oxide films varies greatly, and has been estimated to be from several microns to a millimetre [Campbell 2000]. Many authors [Green and Campbell 1994, Cao 2001] studied a difference of oxide films using Energy dispersive X-ray analysis (EDX) and showed that, compared to young films, the old oxide films had a significantly higher peak of oxygen showing greater amount of oxide or thicker characteristic of the old oxide film. Old oxide films may have formed at different stages in the melting process. They may originate from the original ingots (formed in the electrolytic cells used in the Hall-Heroult process), or from reaction between the melt and the atmosphere or the

refractory lining during melting, holding and transfer, etc. Moreover, old oxide films can be observed in a casting with a long solidification time. Old oxide films are stable and if care is not taken to remove them, they can be carried through the entire life of the molten alloys until discovered in the end product, the casting.

Table 2.2 Characteristics of oxide films formed in the castings process.

Type of film	Growth time	Thickness (μm)	Description	Reference
Young oxide films	<0.01 s	0.056 – 0.127	Observed only as change in apparent colour of melt surface	[Agema 1989]
	0.01-1 s	0.05 – 0.50	Delicate, transparent, thin film, with sharp creases or wrinkles	[Divandari and Campbell 2001]
Old oxide films	10 s to 1 min	10	Flexible, extensive films	[Campbell 2000]
	10 min to 1 hr.	100	Thicker films, less flexible	[Campbell 2000]
	10 hr. to 10 days	1000	Rigid lumps and plates	[Campbell 2000]

2.1.3 Entrainment of oxide films in castings

The surface oxide film on an aluminium alloy melt acts at a protector from either oxidation or diffusion of gas into the underlying metal. The oxide film is therefore not harmful as long as it continues to be a surface film. The problem with the surface film only occurs when it becomes a submerged film.

During pouring or stirring of the melt, the surface film may be broken or folded over with a dry side lying against a dry side. These folded films will trap gas between them and then entrain into the bulk of the melt. Clearly, the side of the film which grew on the liquid surface is wetted by the melt, whereas the opposite side is presented to air (a mixture of N_2, O_2, Ar, etc.). On the one hand, the film which continues to be wetted is

strongly bonded with the liquid metal when the metal solidifies, and on the other hand, the dry interfaces of the oxide films separated by the residual entrained gas form a crack. After solidification, these folded oxide films will act as cracks in the final casting known as a double oxide film defects [Cao and Campbell 2000]. It is commonly the case that cast aluminium alloys readily contains oxide films [Mi et al. 2004]. Figure 2.2 shows an example of a double oxide film defect observed in the cast Al-Si-Mg alloy. The doubled nature of oxide film defect is shown by the symmetrical oxide film on the both sides of the fracture surfaces.

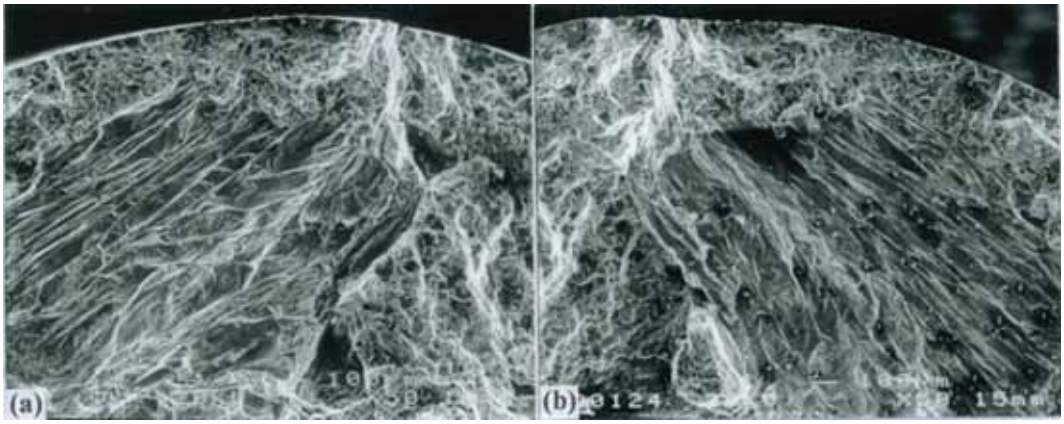

Figure 2.2 The SEM images showing the double oxide film defect on fracture surfaces of the cast aluminium alloy. [Cao and Campbell 2001]

The entrainment of surface oxide films into the bulk of the melt occurs for a number of reasons as follows;

2.1.3.1 Surface turbulence

Surface turbulence is perhaps the most common mechanism to submerge surface oxide film and then incorporate it into the melt. Since oxide films have deformability and flexibility, they will be compressed or bent by the surface turbulence. During such actions as pouring, splashing, and stirring, the surface oxide films may also be broken

and the new oxide film will form on the freshly exposed surface of the liquid metal. All actions fold the surface film, overrun it with the liquid metal, and submerge it. Figure 2.3 shows the folding action of the surface caused by the surface turbulence. It can be seen that the formation of a folded film or double oxide film defect may consist of thick old oxide film, or new thin oxide film, or both of them.

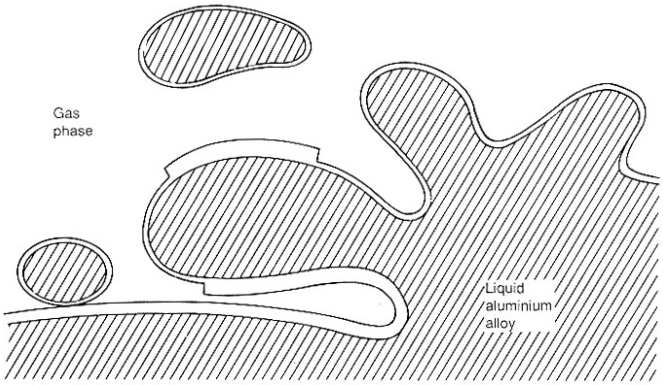

Figure 2.3 Schematic view of surface turbulence showing the formation of a folded oxide film [Campbell 2003].

Improper design of the gating system in a gravity poured mould often results in the surface turbulence of the liquid aluminium during filling of the mould, leading to entrainment of the folded oxide films into the melt [Campbell 1993]. The incorporation of random folded double oxide films can be prevented by ensuring that the velocity of the liquid metal in the mould never exceeds a critical velocity, if it does, then the breaking of the surface by droplet formation, or by jetting, or by the breaking of a wave etc., will fold in the surface oxide film. Several researches were carried out to investigate the velocity of liquid metal leading to the generation of surface turbulence during liquid metal filling. It was found that, for aluminium bronze, the critical velocity was 0.4 m/s [Halvaee and Campbell 1997], while it was 0.5 m/s for aluminium alloys [Runyoro et al. 1992]. Campbell [1993] reported that keeping metal velocities below a critical velocity of 0.35 to 0.5 m/s would avoid the possibility of the metal falling back under gravity entraining its oxide film for all liquid metals.

2.1.3.2 Pouring

Oxide films may be entrained into the melt during the pouring of molten alloys. Figure 2.4a shows that the surface film on a liquid metal grows rapidly as it forms as a tube around the falling stream. When the height of the falling stream increases, the oxide film tube will form a dross ring as shown in Figure 2.4b. This represents a loss of metal on transferring liquid aluminium and dross-forming alloys but it is not clear whether the oxide films are also dragged beneath the surface and entrained. In the case that the melt is poured with greater speed and from greater heights, oxide films on the surface of molten alloys can be carried under the surface, together with entrained air as shown in Figure 2.4c.

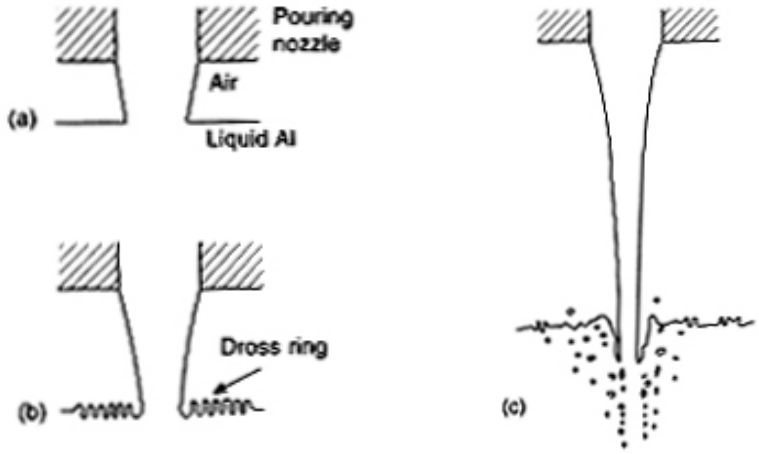

Figure 2.4 The effect of increasing height on a falling stream of liquid showing a) the oxide film remaining intact, b) the oxide film being detached and accumulating to form a dross ring, and c) the oxide film and air being entrained in the bulk melt [Campbell 2003].

2.1.3.3 Surface flooding

Figure 2.5 illustrates another mechanism for the entrainment of oxide films into the melt. The underside of the film grown on a liquid metal is well wetted. However, the top

surface is dry. When an advancing liquid front is stopped for any reason, allowing the liquid metal to flood over the film, the dry sides of the films come into contact and form a double oxide film defect in the melt.

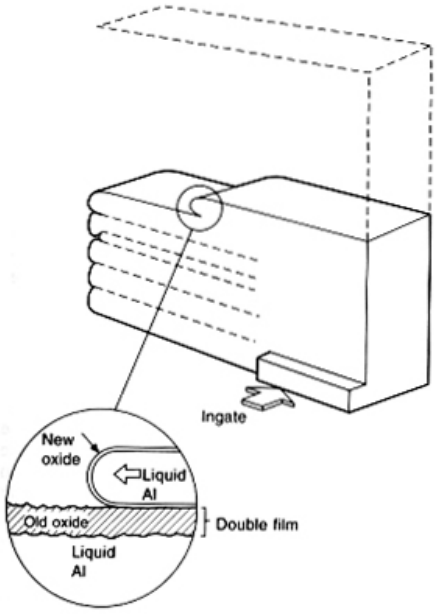

Figure 2.5 The formation of laps and flooding over a surface oxide film [Campbell 2003].

2.1.3.4 Bubble trail

Another oxide film defect formed in the melt is known as a 'bubble trail'. The bubble trail was described by Campbell [2000] as the defect remaining in film-forming alloys after the passage of a bubble through the melt. Divandari and Campbell [2001] explained that the main sources of bubbles in castings are; 1) Poor running system design causing surface turbulence in the metal flow leading to entrained air bubbles. 2) Thermal interaction between the molten metal and the mould or core. (Bubble trails from core blows are usually characterised by a thick and leathery double oxide skin (Figure 2.6a), which is probably why core blows result in leak defects through the upper sections of castings), and 3) Chemical interaction between the molten metal and the mould or core materials. Bubbles arising as a result of gases diffusing into castings rarely cause the

bubbles to grow sufficiently large to become detached, and thus mobile. The bubbles from cores rise through the casting and generally become trapped under the top solidified skin of the casting as shown in Figure 2.6b. The bubble trail is a form of double oxide film defect that is dependent on the splitting and reforming of the oxide film on the upper half of the bubble. Three forms were described. The first form is an open tube, which is observed in highly viscous, semi-solid metal. The second form is a partially collapsed tube that is formed in a lower viscosity metal, where the fraction of solid present is low. The third form of bubble trail is a loose, practically formless tangle which can be found in a turbulently filled casting. The bubble trail could be an important source of other problems, especially leak tightness, in a casting [Divandari and Campbell 2003].

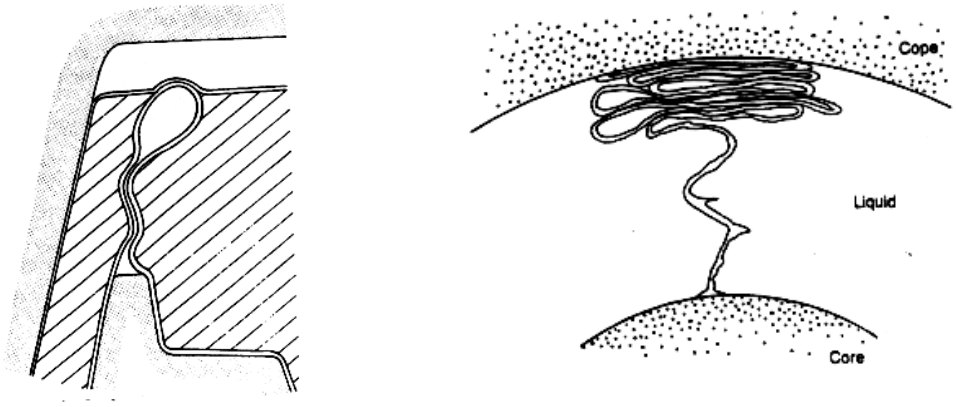

(a) (b)

Figure 2.6 (a) The detachment of a bubble from the top of a core (b) A bubble trail, ending in an exfoliated dross defect [Divandari and Campbell 2001].

2.1.4 Effects of oxide films on mechanical properties

The oxide film formed on the surface of molten aluminium alloy is a chemically stable substance at the temperature commonly used in most cast aluminium alloy operations. It can be entrained into the melt by surface turbulence, frozen into castings, and acts as a crack after solidification. The presence of oxide film defects is practically unavoidable in the cast aluminium foundry. Even if the atmosphere during pouring was designed to be

as inert as possible, these oxide films would be contaminated by the gases and vapours released from the mould, in the case of a green sand mould, as it outgases during filling [Mi et al. 2003]. These oxide films are difficult to measure from both a qualitative and quantitative point of view. Their presence, therefore, can make the mechanical properties, particularly the tensile behavior of castings, unpredictable [Caceres and Selling 1996, Liu et al. 2003].

Since folded oxide films are known to be all sizes and shapes, the cracks in the liquid can clearly be extremely serious, constituting by far the largest defects in a casting. They can form as the majority area of the cross section of castings, causing a major reduction in strength or fatigue resistance [Campbell 2000]. Green and Campbell [1994] used the Weibull distribution to characterize the distribution of fracture strengths of castings produced in an Al-7Si-Mg alloy. They used different runner system designs to produce different levels of surface turbulence, and hence different amounts of double oxide film defects in the castings. In the castings that had greater surface turbulence, the extensive network of oxide films was observed as shown in Figure 2.7 and this crack-like defect appear to directly affect the tensile properties of the casting. The results also showed that the tensile strength distribution was controlled by the level of folded oxide film defects contained. Mi et al. [2004] also used the Weibull distribution to investigate the effect of entrained oxide films on the tensile properties of aluminium alloy. They concluded that oxide films were responsible for much of the scatter in mechanical properties. The entrained double oxide films acted as cracks, significantly reducing the reliability or reproducibility of the strengths of castings.

Oxide films are also thought to be the initiator of fatigue cracks in the casting. Nyahumwa et al. [1998] showed that there was a competing mechanism for fatigue crack initiation in surface turbulently filled castings between a combination of young and old oxide film defects, and pores associated with young oxide films. Their results were supported by Dai et al. [2003] who also found the same evidence in cast Al-7Si-Mg alloy. They stated that entrained oxide films were frequently accompanied by different casting defects such as porosity and cracks. In addition, the increase in oxide film defect sizes directly decreased the mechanical properties of castings [Wang et al. 2001].

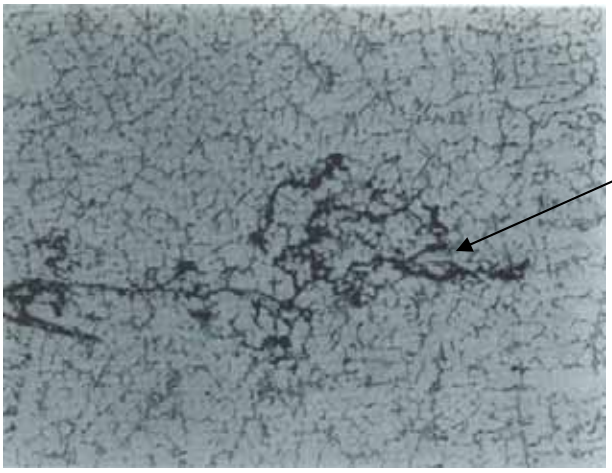

Figure 2.7 large crack-like defects observed in the cast Al-Si-Mg alloy [Green and Campbell 1994].

Beside the reduction in mechanical properties and the reliability of castings, oxide films also result in a variety of problems in the solidification process and in the final casting, for example, 1) the restriction of feed metal during solidification by oxide films or oxide inclusions results in a loss of fluidity and feeding [Eckert Jr. 1992], 2) folded oxide films can provide leakage paths by connecting wall-to-wall in castings [Campbell 2000], and 3) reduction in machinability due to the hard nature of the oxide inclusion [Fuoco et al. 1999, Makarov et al. 1999]. Oxide film, therefore, are detrimental to castings since they play a major role, both directly and indirectly, in reducing the mechanical properties of cast aluminium alloys.

2.1.5 Oxide film removal techniques

Many researchers, recently, have studied methods for minimizing oxide films in cast aluminium alloys. Campbell [2000] suggested that the best way to reduce oxide films in castings was to filter the metal in the running system, after pouring, but before the metal enters the mould. Different kinds of filters are used in the foundry, such as woven glass cloth and steel wire mesh, however they can only remove large inclusions [Makarov et al. 1999]. Recently, ceramic filters, which are extruded, pressed or foam types, have been

widely used in foundries. Ceramic filters are produced in a variety of sizes and shapes, and can be used for filtering bulk metal in the dispensing wells of holding furnaces or within the mould cavity. They have found extensive application in sand, investment, and low pressure die casting process. Ceramic foam filters and fine mesh steel screens at the gate of the mould are commonly used in the production of aerospace castings [Sigworth et al. 1989]. Several researches have shown that filters result in a reduction in oxide film inclusions in the poured metal and control the flow of liquid metal to ensure that the flow conditions in the mould will not reintroduce the entrapment of surface oxide films [Zadeh and Campbell 2002, Dai et al. 2003].

Fluxing is another method to remove oxide inclusions during melt preparation. Fluxes (often based on a chloride or fluoride) are added into the melt in order to agglomerate with undesirable constituents and form dross or slag, which will rise to the surface and can be removed by skimming. Fluxing can perform single or, in combination, various functions, for example, degassing and refining [Davis 1993]. Several types of fluxes are used in aluminium alloy castings. Covering fluxes, which form a liquid cover on the surface of melt, is used to reduce oxidation and prevent gas absorption [Zalensas 1993]. Cleaning flux contains a chloride salt compound and a fluoride to facilitate wetting of the oxide inclusions for easier separation from the melt [Davis 1993]. Drossing flux is designed to promote separation of aluminium oxide dross layer from the melt to avoid excessive metal loss [Zalensas 1993]. Fluxes can be manually added on the melt surface but they have limited contact with impurities in the melt. The flux injection technique, therefore, has been introduced by delivering controlled amounts of fluxes into the melt in inert gases (such as nitrogen or argon). The small bubbles with adhering flux introduced offer a large specific surface area and the oxide particles will be swept to the melt surface by flotation where they accumulate in the dross. During fluxing, hydrogen can also diffuse from the melt into the rising gas bubbles causing a reduction of hydrogen content in the melt. Therefore the flux injection techniques are widely used throughout the casting industry, because the treatment is effective and it reduces both gas content and inclusion content.

The latest method, suggested by Cao and Campbell [2003], is the precipitation of intermetallic compounds on suspended oxide films. Their results showed that there was an improvement in the cleanliness of the melt after the melt was held at a temperature suitable for intermetallic precipitation for a few hours, which was, in turn, associated with an improvement in the mechanical properties of castings. However, this method has to be studied more to determined its feasibility in the foundry.

2.2 Porosity in cast Al-Si-Mg alloys

The presence of porosity is usually unavoidable to a certain extent in any casting, and can have a detrimental effect on the mechanical properties and surface quality [Samuel and Samuel 1992]. Porosity in castings can be classified by the size of the pores, and divided into macroporosity (a pore larger than the dendrite cell size e.g. about 100 μm or bigger [Caceres 1995]) and microporosity (pores less than 100 μm). Porosity has also been divided by the cause, being formed as either gas porosity or shrinkage porosity [Lee et al. 2001]. The first type, gas porosity (hydrogen porosity), is the term given to porosity that is generally rounded, isolated, and well distributed as shown in Figure 2.8a. This kind of pore is caused by the rejection of dissolved hydrogen because of its lower solubility in the solid state. The second type is interconnected or clustered and of an irregular shape, corresponding to the shape of the interdendritic region, (see Figure 2.8b), and is usually termed shrinkage porosity [Piwonka and Flemings 1966, Chiesa et al. 2001, Sabau and Viswanathan 2002]. Shrinkage porosity is a result of the inability of the casting to feed the required amount of metal during the contraction from liquid to solid. In general, beside the precipitation of hydrogen gas or the inadequate feeding of volumetric shrinkage, porosity in cast aluminium alloys is usually likely to occur by the combined effects of both causes [Rooy 1992, Atwood and Lee 2002, 2003].

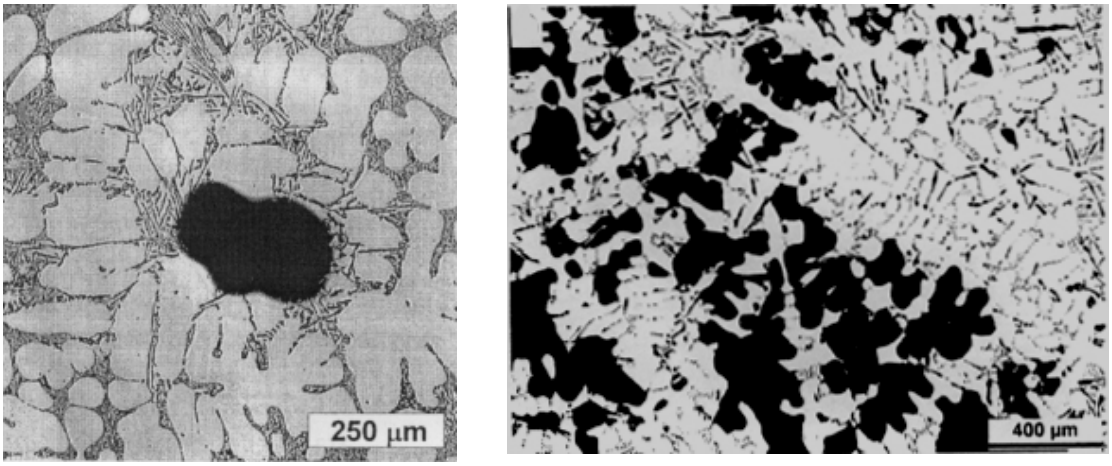

(a) (b)

Figure 2.8 Micrographs showing a) gas porosity [Anson and Gluzleski 1999] and b) shrinkage porosity in Al-Si-Mg alloys [Dinnis et al. 2004]

2.2.1 Gas porosity

2.2.1.1 Hydrogen gas evolution

Hydrogen is the only gas with measurable solubility in aluminium. Therefore, increasing initial hydrogen content directly results in an increase in gas porosity in cast alumnium alloys [Atwood et al. 2000]. Molten aluminium readily absorbs hydrogen from the atmosphere by this reaction:

$$2Al_{(l)} + 3H_2O_{(g)} = Al_2O_{3(s)} + 6H_{(g\ in\ l)} \quad (2.1)$$

Charge materials are common sources of hydrogen absorption in melts prepared for casting. The most usual contaminants are hydrated corrosion products, water and oil, on the surfaces of virgin metal stored under unsatisfactory conditions, and on secondary metal and process scrap returned for remelting. One further important source of hydrogen is steam evaporated from residual moisture in the linings of launders, moulds, and their accessories over which the molten metal passes during transfer from the furnace in the casting operation. In green sand castings, the source of hydrogen is

reaction between the solidifying metal and steam generated when moisture in the mould is vaporized at the sand face [Talbot 1975].

The absorption and desorption of hydrogen from aluminium are impeded by the oxide skin on liquid aluminium. Weigel and Fromm [1990] measured the rate of hydrogen absorption and desorption in quiescent melts and in melts with an agitated surface where oxide films were removed. They conclude that undamaged Al_2O_3 films act as a barrier to the absorption of hydrogen at temperatures below 800 ^oC (absorption rate is only a few ml/m^2 hr), although the effect is reduced for desorption of hydrogen from the melt. The absorption rate increases to the range of $10^4 - 10^5$ ml/m^2 hr when the oxide skin is removed. Thus both the water vapour pressure in the air and the state of the surface oxide will control hydrogen content of the melt.

The solubility of hydrogen in aluminium has been measured by many researchers. Ransley and Neufeld [1948] showed that the maximum solubility of hydrogen in the solid is about 0.0175 ml/ 100g at the melting temperature of pure aluminium metal [Han and Viswanathan 2002]. Talbot [1975] stated that the solubility of hydrogen in aluminium at 660 ^oC (melting temperature) are 0.7 and 0.04 ml/100g for the liquid and solid respectively. Since the solubility of hydrogen is less in the solid than in the liquid metal, some of the gas is rejected from solution and is entrapped in the solid structure. Figure 2.9 shows the solubility of hydrogen in molten aluminium [Ranley 1948].

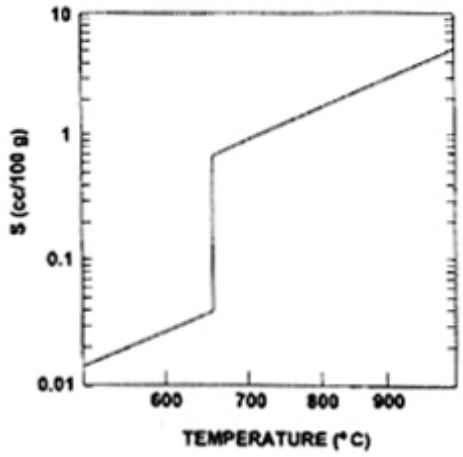

Figure 2.9 Solubility of hydrogen in molten aluminium [Ranley 1948].

The diffusivity of hydrogen in solid aluminium has been measured by many authors, with good agreement between their results. Eichnauer and Markopoulous [1974] fitted expressions to their data for both the solid and liquid states:

$$D = 1.1 \times 10^{-1} \cdot \exp(-4922/T)\ cm^2/s, \qquad [633K < T < 873K] \qquad (2.2)$$

$$D = 3.8 \times 10^{-2} \cdot \exp(-2315/T)\ cm^2/s, \qquad [1053K < T < 1273K] \qquad (2.3)$$

where D is the diffusion rate of hydrogen. Hydrogen has a diffusion coefficient higher than that of aluminium in liquid aluminium by two orders of magnitude. Hydrogen is a highly mobile solute that is partitioned at the solidification front reaching high levels of supersaturation and it therefore plays a key role in the formation of porosity upon solidification. Talbot [1975] showed that during a heat treatment at 550 ^{o}C, hydrogen in cast aluminium could continue to diffuse into pores in the solid state since pores became larger and fewer.

2.2.1.2 The nucleation of gas porosity

A number of authors have studied the nucleation of pores during solidification of aluminium alloys. There is a classification scheme for types of bubble nucleation based upon the study of bubbles forming in several different systems, which is summarized as follows;

2.2.1.2.1 Homogeneous nucleation

A description of the formation of pores in liquid was derived by Fisher [1948] for the case of homogeneous nucleation. It was explained in terms of a quantity of work associated with the formation of a bubble in the liquid. The formation of a bubble of volume V required work of P_eV, meaning that porosity had to push back the liquid to create a pore of volume V, where P_e was the pressure of the liquid. The formation of the new liquid/gas interface of area A required a quantity of work of γA, where γ was the interfacial energy or surface tension (N/m). The work required to fill the bubble with gas at pressure P_i was $-P_iV$. This work was negative since the pressure inside the bubble

clearly helped the formation of the bubble. Campbell [2000] demonstrated that the work (free energy) required for the formation of a spherical vapour bubble of radius *r* following the approach by Fisher was:

$$\Delta G = \gamma A + P_e V - P_i V \qquad (2.4)$$
$$= 4\gamma\pi r^2 + 4/3\ \pi r^3\ (P_e - P_i)$$

where P_e - P_i is the pressure difference between the exterior and the interior of the bubble, (ΔP). As with dense phase nucleation, a plot of free energy versus bubble radius *r* shows a maximum which constitutes an energy barrier to nucleation. This critical radius for nucleation is:

$$r_c = 2\gamma/\Delta P \qquad (2.5)$$

Solving this equation using the properties of Al-Si-Mg alloy, where surface tension is about 0.9 N/m, and assuming a critical bubble radius of about two atomic diameters of aluminium (of about 0.58 nm). The pressure required for homogeneous nucleation, therefore, should be around 31,000 atmospheres.

Wilt [1986] applied the work of Blander and Katz [1975] to the water carbon dioxide system. Their work differed from Fisher's in that they used the Zeldovich formation for the coefficient of the nucleation rate equation. They determined an equation that, when the suggested approximations were made, was similar to Fisher's. Using the data for the aluminium-hydrogen system, a required pressure of 31,500 atmospheres could be calculated.

In summary, investigations of the homogeneous nucleation of pores in liquid metals have shown that the initiation pressure that is required for nucleation is extremely high and that, therefore, homogeneous nucleation is unlikely to occur in practice.

2.2.1.2.2 Heterogeneous nucleation

Fisher also considered the case of the nucleation of a bubble against the surface of a solid substrate. The liquid was considered to make an angle θ with the solid. This contact angle defines the extent of wetting; $\theta = 0^o$ means complete wetting, whereas $\theta = 180^o$ means complete non-wetting (see Figure 2.10). Fisher showed that nucleation was easier by a factor of:

$$P_{het}/P_{hom} = 1.12\ [(2 - \cos\theta)(1 + \cos\theta)^2 / 4]^{1/2} \qquad (2.6)$$

Figure 2.11 shows the fraction of P_{het}/P_{hom} calculated by Equation 2.6 derived by Fisher. It indicates that, as the contact angle increases to 180^o, any difficulty of heterogeneous nucleation should fall to zero. In fact, perfect non-wetting is impossible and the maximum contact angle attainable in practice is perhaps close to 160^o. Campbell [2000] calculated that the required pressure for heterogeneous nucleation in Al-Si-Mg alloys was reduced to around 1500 atmospheres. Although the pressure required for heterogeneous nucleation is $1/20^{th}$ of that of homogeneous nucleation, it is still too high to be reached in a usual solidification process.

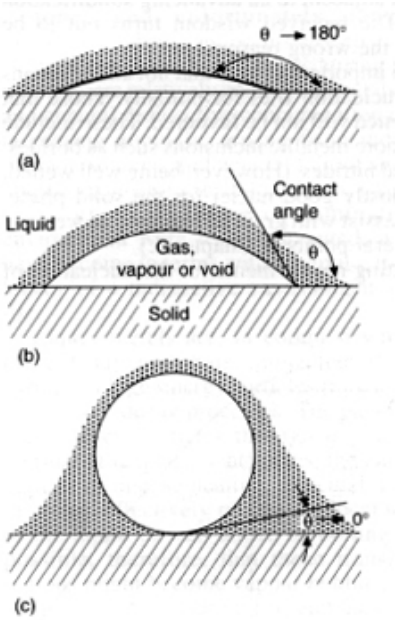

Figure 2.10 Geometry of a bubble in contact with a solid showing a) poor wetting, b) medium wetting, and c) good wetting. [Campbell 2003]

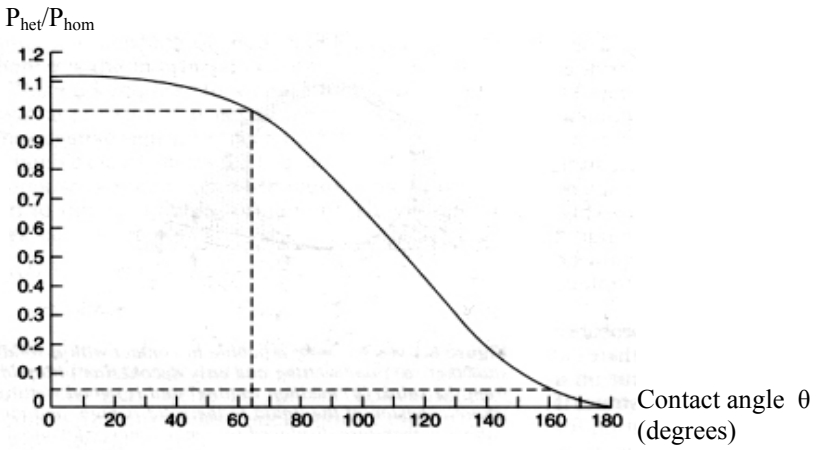

Figure 2.11 The relative difficulty of nucleating a bubble as the contact angle with the solid changes from wetting to non-wetting. [Campbell 2003]

Wilt [1986] demonstrated the effect of contact angle for heterogeneous nucleation on smooth planar interfaces in the water-carbon dioxide system. A supersaturation of five was common for freshly opened carbonated beverages, which would correlate to a contact angle of approximately 175^o. He extended the calculation to conical and spherical cavities as shown in Figure 2.12 and showed that, at the low supersaturation value of five, nucleation would occur in conical cavities with a subtended angle of 30^o if the contact angle was 130^o. This therefore suggested that the heterogeneous nucleation might be possible if the bubble formed on the conical cavities or the rough surface of inclusion in the melt. However, this calculation has not been verified experimentally in cast aluminium alloys, nor has it been confirmed theoretically by other authors.

Several researchers suggested that nucleation of bubbles in molten metals may occur on entrapped oxides. Shahani [1985] added Al_2O_3 particles to Al-Si alloys and found that the percentage porosity increased. Laslaz and Laty [1991] found oxides on the surfaces of pores in aluminium castings using a SEM. They also found that increasing the number of inclusions increased the percentage porosity and altered the pore morphology to a more spherical shape, which was suggested indicated earlier nucleation. The experimental evidence pointed to Al_2O_3 particles acting as nucleation sites for bubble formation. Surface tension values for the Al-Al_2O_3 system vary over a tremendous range

depending on the measurement technique but Eustathopoulos et al. [1985] found a contact angle of 150^o at 700 ^{o}C. The contact angle increased with decreasing temperature, making Al_2O_3 an excellent nucleation substrate. Kato [1999] reported that non-wetted surfaces on surfaces of oxide inclusions in the liquid metal might act as the nucleation sites of porosity in the castings. He suggested that the contact angle between Al_2O_3 and liquid Al was 150^o, and that pores were formed heterogeneously on the surfaces of oxides when the pressure in the liquid at the solid-liquid interface was about 2.7 atm. However, this assumption seems to be unlikely because, referring to the nucleation of a pore on a smooth planar interface, according to Equation 2.6, the pressure required for heterogeneous nucleation with a contact angle of 150^o is more than 3000 atm. Nucleation might be possible, if the surface of the oxide inclusions were rough or had some conical cavities as suggested by Wilt but it still needs to be confirmed by the experimental results. The researches carried out to study the nucleation of pore in aluminium alloys castings recently, therefore, suggested that both homogeneous and heterogeneous nucleation are very difficult in practice.

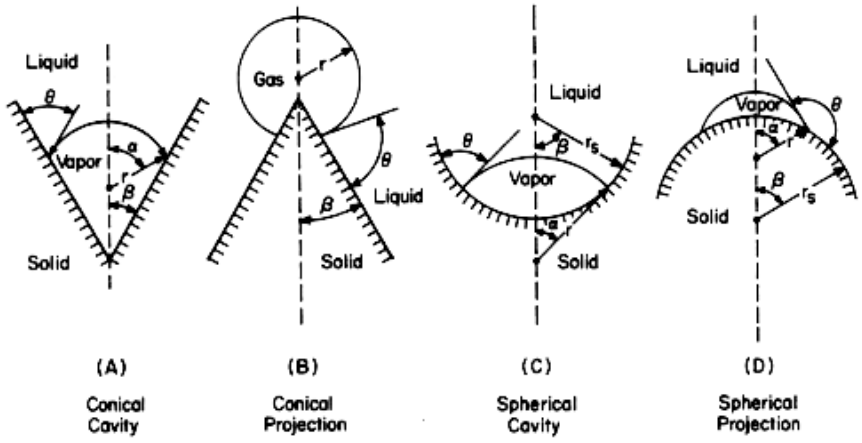

Figure 2.12 Definition of geometrical parameters for heterogeneous nucleation [Wilt 1986].

2.2.1.2.3 Nonclassical nucleation

According to equations 2.5 and 2.6, the pressure required for both homogeneous and heterogeneous nucleation of pore are extremely high; many authors, therefore, have

researched other theories in order to describe the formation of porosity in cast aluminium alloys [Chen and Engler 1994, Jones et al. 1999, Fox and Campbell 2000, Campbell 2003]. One of the most common mechanisms by which bubbles form is by the growth from pre-existing gas bubbles entrained in the melts. Chen and Engler [1994] proposed that for a conical cavity on the surface of a solid inclusion a gas pocket would have an existence. Fox and Campbell [2000] reported that double oxide films containing nonsoluble gas (air) between the two dry sides of the films and entrained into the melt during pouring or mould filling, were seen to possess the potential to initiate pores with negligible difficulty. Since no nucleation event was required, only growth from the atmosphere trapped between the oxide films, the supersaturation required is directly related to $2\gamma/r$. Therefore, the growth of pre-existing gas-filled cavities is likely to be the most probable sites of pore formation.

2.2.2 Shrinkage porosity

Shrinkage is caused due to the density difference between solid and liquid alloy phases. The solidification of pure aluminium is accompanied by a 7% decrease in volume during the phase change form liquid to solid. Common aluminium casting alloys exhibit volumetric shrinkages in the 5 to 6% range [Anson and Gruzleski 1999]. As solidification progresses, metal that is still fluid will try to flow to compensate for the liquid/solid volume change. However, the ability to feed becomes more and more difficult due to the decreasing size of the channels along which feeding take place, that is, the interdendritic network. Eventually the channels freeze completely, isolating small areas from a supply of fresh metal. At this point any shrinkage occurring in these isolated areas causes a tension within the liquid, and voids may form to relieve this tension [Lee et al. 2001]. A single shrinkage pore will appear as a group of smaller pores due to the sectioning of the various ‘arms’ of the shrinkage pore (see Figure 2.8b). The size of individual microshrinkage pores may range in length from a few microns to a few millimetres.

The possible feeding mechanisms are divided into five categories [Campbell 2000], as shown in Figure 2.13 and Table 2.3. Liquid and mass feeding provide compensation for

shrinkage contraction with little resistance to flow while burst feeding has not been widely studied. Solid feeding has been studied using stress analysis, and can been seen in many poorly designed castings as surface shrinkage. Among five possible feeding mechanisms, interdendritic feeding is considered to be one of the most difficult stages particularly in long freezing range alloys. Feeding becomes progressively difficult since interdendritic channels continuously decrease during solidification. It, therefore, plays a major part in the formation of shrinkage porosity in the interdendritic regions.

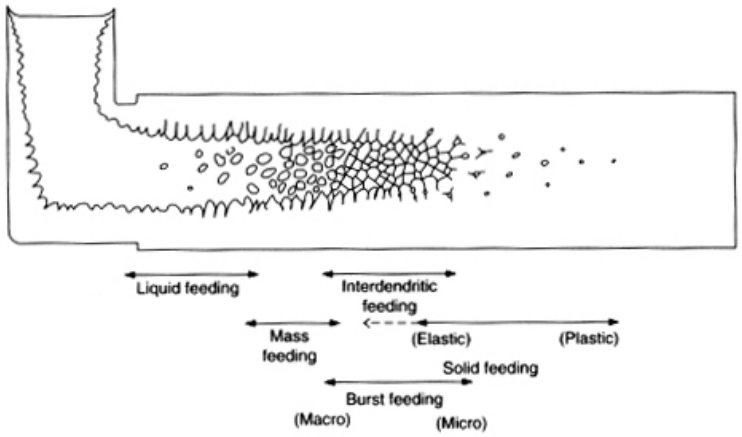

Figure 2.13 Feeding mechanisms in the casting during solidification [Campbell 2000]

Table 2.3 Five mechanisms of feeding occurred during solidification [Campbell 2000]

Feeding	Mechanisms
Liquid feeding	Bulk motion of the molten metal.
Mass feeding	Combined bulk flow of liquid and equiaxed grains as a slurry.
Interdendritic feeding	Interdendritic fluid flow in the channels between primary dendrites/cells during solidification.
Burst feeding	Discontinuous feeding when the dendritic network collapses locally and residual fluid flows inward.
Solid feeding	Elastic and plastic deformation of the solid.

2.2.2.1 The nucleation of shrinkage porosity

The problem of the nucleation of shrinkage porosity has also been widely discussed. The presence of shrinkage porosity is thought to occur in an unfed isolated volume of liquid because the concept of shrinkage means that there is a decrease in volume because of the density change associated with phase transformation. However, the nucleation of shrinkage porosity can be explained as a nucleation of gas porosity following the approach by Fisher. Instead of the diffusion of gas atoms to the pore, it can be considered as the diffusion of vacancies. As described in sections 2.2.1.2.1 and 2.2.1.2.2, the pressures required for nucleating porosity in both homogeneous and heterogeneous cases are very high. Therefore it is unlikely to occur in practice.

Pehlke [1987] showed that there was an association between gas porosity and shrinkage during solidification since porosity formation was observed to nucleate at the base of dendrite arms. To consider the nucleation of a combined gas and shrinkage pore, consider there is gas at pressure P_g on the inside of the pore effectively pushing, and a negative pressure P_s in the bulk liquid effectively pulling, then Equation 2.4 can be recalculated as;

$$2\gamma/r_c = P_g + P_s \tag{2.7}$$

Although the additional pressure from dissolved hydrogen gas may support the nucleation of shrinkage porosity, these pressure are still not high enough to nucleate a pore in practice. Therefore, the most probable sites of shrinkage porosity formation are entrained double oxide films or pre-existing pores.

2.2.3 Growth of porosity

As mentioned in the previous sections porosity forms due to the effects of hydrogen rejection and solidification shrinkage, either individually or in combination. After porosity formation during solidification, their growth will depend on the pressures at the pore interface, as follows;

$$P_g + P_s \geq P_{atm} + P_H + P_{s\text{-}t} \quad (2.8)$$

Where P_g is the equilibrium pressure of the dissolve gas, P_s is the pressure drop due to solidification shrinkage, P_{atm} is the atmospheric pressure, P_H is the pressure due to the metallostatic head, and $P_{s\text{-}t}$ is the pressure due to pore-liquid surface tension. [Samuel and Samuel 1992, Lee and Hunt 1997, Atwood et al. 2000, Lee et al. 2001, Dinnis et al. 2004]. In this balance, the metallostatic pressure can be ignored because it has insignificant influence on this mechanism compared to the other pressures. Therefore, the porosity will grow when it overcomes the surface tension and pushes away the aluminium with the support of segregation that locally increases hydrogen content and the negative pressure created by shrinkage. In general, the growth of the pore can be controlled by two mechanisms. The first occurs in a casting with sufficient feeding and the second occurs in the casting without feeding. If there is sufficient feeding, the growth of porosity will be controlled by only the rate of gas deposition. In the case of poor feeding, the growth rate will be controlled by shrinkage and deposition of hydrogen gas in combination.

The formation of porosity is also significantly influenced by process variables, such as cooling rate, grain structures, alloy chemistry and the presence of inclusions [Mohanty et al. 1995]. Several reports have showed that increasing solidification rate decreases porosity size [Lee and Hunt 1997]. Atwood et al. [2000] found that increasing the solidification velocity reduced the pore size whilst increasing the pore number density. At a low solidification velocity, (of about 10 ^{o}K/s), the pore is rounded, while at a medium velocity the pore was found to have grown between the primary dendrite arms along the grain boundaries. At a high velocity (of about 47 ^{o}K/s), the pore is constricted also between the secondary dendrite arms. Shivkumar et al. [1990] also showed that the size of pores in a casting decreased exponentially with increased cooling rates. They suggested that the strong effect of cooling rate may have originated because the density of pores is proportional to the density of grains. It has been established that the density of grains is sensitive to cooling rate during solidification. Thus, the density of pores is also a strong function of cooling rate because, when the grain size is small, growth of pores is inhibited because of space constrictions.

2.2.4 Effects of porosity on mechanical properties

Porosity is a leading cause in the reduction of mechanical properties, particularly elongation and fatigue resistance, as well as a loss of pressure tightness and a degradation of the surface appearance in cast parts [Anson and Gruzleski 1999]. Basically, porosity results in a discontinuity in the castings and a reduction in load bearing area. Eady and Smith [1986] also showed that pores could act as stress concentrators, initiation sites for fatigue cracks, and reduce tensile properties, particularly elongation.

Turner and Bryant [1967] measured the tensile properties of plates hot rolled from semicontinously cast ingots of an Al-Cu-Mg-Si alloy and obtained a good correlation between these and the gas porosity in the ingots. Figure 2.14a illustrates some of their results. Another example of the deleterious effect of gas porosity on mechanical properties in sand cast 356-T6 aluminium alloy obtained by Traenkner [1982] is shown in Figure 2.14b.

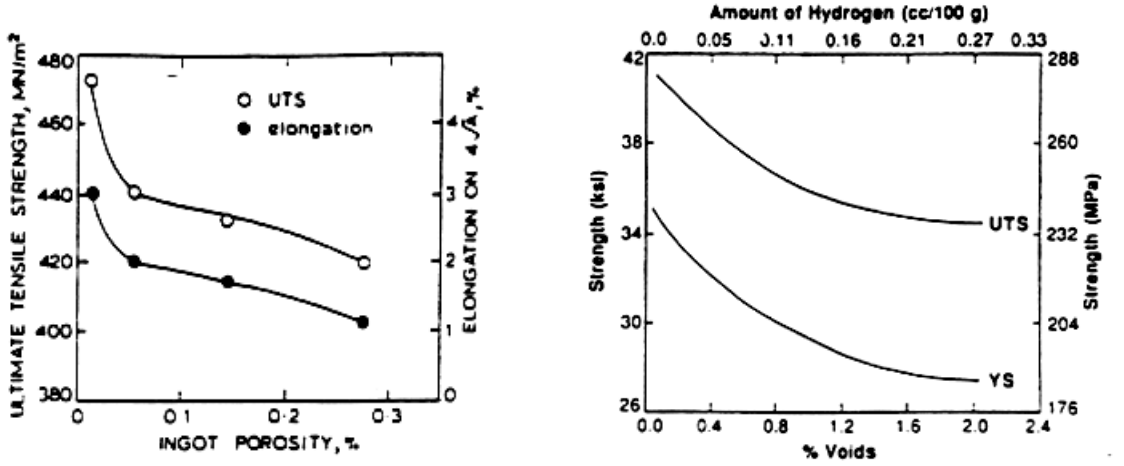

Figure 2.14 Effect of porosity on tensile properties obtained from a) cast Al-Cu-Mg-Si alloy [Turner and Bryant 1967] and b) sand cast Al-Si-Mg aluminium alloy [Traenkner 1982].

Several authors showed that the reduction in the ultimate tensile strength of aluminium alloys did not relate to the average volume fraction of porosity. Instead, a better correlation was obtained with the length or the size of the pore in the cross-section surface [Herrera and Kondic 1977, Surappa et al. 1986]. They also reported that, when the castings contained large porosities, the relative decrease in tensile strength was larger than predicted by the reduction in the load bearing area. Griffin et al. [2003] studied the effect of porosity detected by non-destructive evaluation techniques on the mechanical properties of cast aluminium alloys. They found that ultimate tensile strength (UTS), strain to failure, and fatigue properties of the castings were significantly affected by relatively small amounts of porosity. UTS values decreased from 403 MPa to 338 MPa when porosity with diameters in the range of 0.25 to 1.0 mm. were present.

2.2.5 Porosity reduction techniques

The only effective methods to limit porosity are to reduce the hydrogen content of the liquid metal and reduce shrinkage, which are the main causes of the formation of pores in cast aluminium alloys. To reduce shrinkage problems, a feeder is used. Many techniques have been developed for degassing molten aluminium alloys. The simplest method is to hold the metal at a lower temperature for some period of time at which the hydrogen solubility is lower and thus provide for natural outgassing. However this is not economic in a foundry. Active degassing of aluminium melts can be accomplished using gas purging, degassing fluxes, or mechanical mixer degassing. One widely used technique uses injection of a purge gas or gas mixture under pressure (argon or nitrogen) through a flux tube, pipe, lance, porous plug, or a rotary impeller degasser. The rotary impeller degasser is by far the most effective method for degassing [Sigworth et al. 1989, Davis 1993]. Other methods with less practical interest include ultrasonic and vacuum treatments [Kaye 1983].

2.3 Fe-rich phases in cast Al-Si-Mg alloys

The main impurities that exist in cast aluminium alloys are iron (Fe), manganese (Mn), copper (Cu) and zinc (Zn) [Villeneuve 2001]. Iron, stemming from impurities in bauxite ore, and contamination with ferrous metals and oxides during handing and recycling, has been known as the most deleterious impurity due to its role in the formation of brittle Fe-rich intermetallic phases. Iron is the most commonly found impurity in cast aluminium alloys since it cannot be economically removed. Dilution is the only practical method to reduce iron and the cost of aluminium alloys, consequently, is inversely related to their iron contents [Crepeau 1995, Li et al. 2004].

The solubility of iron in molten aluminium is quite high, leading to the eventual dissolution of ferrous material in contact with molten aluminium. In contrast, the solubility of iron in solid aluminium is very low, only 0.05 wt% at 660 ^{o}C. Its solubility is even less at room temperature or in the presence of alloying elements that form compounds with iron. Fine Fe-rich intermetallic phases precipitate at intermediate temperatures and cannot be redissolved in the solid state [Crepeau 1995].

The various alloying and impurity elements in an alloy go partly into solid solution and partly form intermetallics during solidification. In the Al-Si-Fe system there are five main Fe-rich phases: Al_3Fe, α-Al_8Fe_2Si, β-Al_5FeSi, δ-Al_4FeSi_2, γ-Al_3FeSi [Mondofo 1976, Skjerpe 1987]. A δ-Al_4FeSi_2 phase is often present in high Si alloys while γ-Al_3FeSi forms in high Fe and high Si alloys. In addition, Fe and Mg may result in the appearance of π-$Al_8Mg_3FeSi_6$. Therefore, α-phase, β-phase and π-phase are normally precipitated in cast hypoeutectic and eutectic aluminium alloys containing magnesium [Cao 2001]. Figure 2.15 shows an example of a microstructure of a cast Al-Si-Mg alloy containing 0.6 wt%Fe.

Backerud et al. [1990] explained that, depending upon the alloy composition, the following main sequence of phase precipitation will occur in Al-Si-Mg alloys;

1) Formation of primary α-aluminium dendrites
2) The aluminium-silicon eutectic reaction

3) Precipitation of secondary eutectic phases

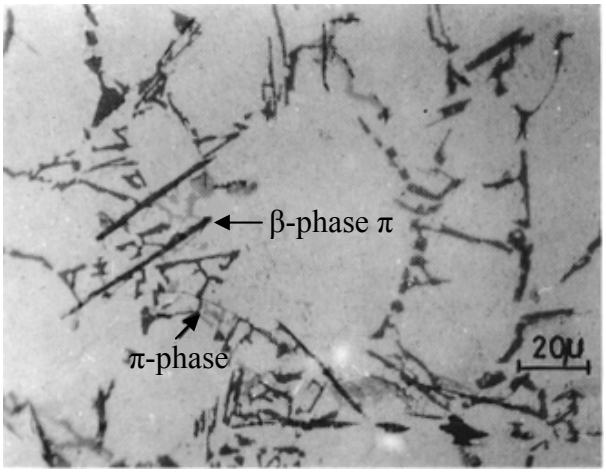

Figure 2.15 Micrograph obtained from cast Al-7Si-0.3Mg-0.6Fe alloy showing the Fe-rich phases in the microstructure [Ravi et al. 2002]

Table 2.4 Reactions during the solidification process of Al-7Si-0.3Mg alloy (A356.2) [Backerud et al. 1990]

No.	Reactions	Temp (^{o}C)
1	Development of dendritic network	< 615
2a	L => Al + Si	
2b	L => Al + Al_5FeSi	
3a	L => Al + Si + Al_5FeSi	575
3b	L + Al_5FeSi => Al + Si + $Al_8Mg_3FeSi_6$	567
4	L => Al + Mg_2Si + Si	555
5	L => Al + Si + Mg_2Si + $Al_8Mg_3FeSi_6$	554

As shown in Table 2.4, the microstructure of Al-Si-Mg alloys can consist of five phases; α-Al, β-Al_5FeSi, π-$Al_8Mg_3FeSi_6$, Mg_2Si and Si. The primary α-aluminium dendrites firstly nucleate and grow as the liquid cools below the liquidus temperature (~ 615 ^{o}C). β-Al_5FeSi phases tend to form thin platelets in the interdendritic and intergranular regions appearing as needles in cross section. This phase is responsible for a significant

decrease in mechanical properties of the alloy since it is very brittle and has relative low bond strength with the matrix [Murali et al. 1995, Taylor et al. 1999].

The addition of magnesium, in amounts of up to 0.5 wt%, to molten Al-Si alloy leads to the precipitation of the age-hardening compound, Mg_2Si, that appears in the form of small black particles formed near the sides of the eutectic Si particles as shown in Figure 2.16 [Samuel et al. 1998]. This compound, when precipitated from solid solution during heat treatment, is responsible for the improvement in mechanical strength. In the as-cast state, magnesium is present as fairly large particles of Mg_2Si. Depending on the cooling rate after solidification, some magnesium is also retained in solid solution. The changes in mechanical properties, an increase in strength, resulting from heat treatment are due to the fine, coherent precipitation of Mg_2Si [Sigworth 1989]. The effect of Mg content on mechanical properties of aluminium alloy was pointed out by Granger et al. [1984], who reported that a 0.01wt% increase in magnesium resulted in an increase of yield strength of about 3.45 MPa in A357 alloys.

Nagel et al. [1983] studied the precipitation of Fe-rich phases in Al-Si-Mg alloys and stated that, at the low iron contents, magnesium precipitates preferentially in the form of Mg_2Si and the π-$Al_8Mg_3FeSi_6$ phase occurred as either a Chinese script-like phase or an indefinite-shaped peritectic phase as shown in Figures 2.15 and 2.16 when iron content increased to 0.6 wt%. Samuel at el. [1998] and Ravi et al. [2002] reported that the increase in iron content from 0.2 to 0.6 wt% resulted in an increasing amount of β-Al_5FeSi phases and the transformation of a large proportion of the β-Al_5FeSi, needle-like phases, into a Chinese script-like phase, with a composition close to $Al_8Mg_3FeSi_6$. Caceres et al. [1999] also found that higher magnesium in Al-7Si alloys resulted in the formation of large $Al_8FeMg_3Si_6$ (π-phase) intermetallic compounds in addition to small particles of β-Al_5FeSi phase.

The equilibrium hexagonal form of α-Al_8Fe_2Si phase is only thermodynamically stable in high purity Al-Si-Fe alloys. Additions of Mn, Cr, Cu, V, Mo and W all promote a body-centered cubic structure for the α-Fe phase [Allen et al. 1998]. When Mn is added, α-$Al_{15}(FeMn)_3Si_2$ phase often has the appearance of the Chinese script form, with its

characteristic large irregular-shaped particles. If iron and manganese combined are above 0.8%, $Al_{15}(FeMn)_3Si_2$ crystals are the primary phase and appear as hexagonal globules although the compound is cubic. These globules do not embrittle the alloy, but appreciably reduce the machinability [Mondolfo 1976].

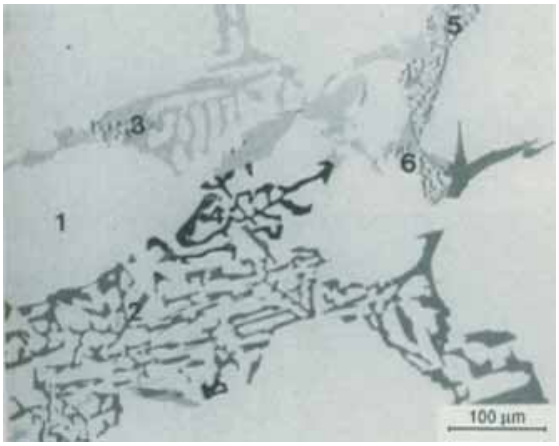

Figure 2.16 Microstructure of cast A319 alloy containing 1.2 wt%Mg showing 1) α-Al dendrite, 2) eutectic Si, 3) $Al_8Mg_3FeSi_6$, 4) Mg_2Si, 5) Al_2Cu, and 6) $Al_5Mg_8Cu_2Si_6$ phase. [Samuel et al. 1998]

In the presence of manganese, the iron compound crystallizes in three distinctly different morphologies, needle-like (β-phase), Chinese script morphology (α-phase), and star-like or polyhedral morphology (primary α-phase), depending on the Fe/Mn ratio and cooling rate. The chemical composition of the primary α-phase is almost the same as that of the Chinese script α-phase, and the chemical formula for this phase can be represented approximately by $Al_{15}(Mn,Fe)_3Si_2$ [Narayanan et al. 1994].

Armstrong [1978] suggested that at low cooling rates, the β-Al_5FeSi phase platelets are thick and precipitate mainly at grain boundaries, leading to serious alloy embrittlement. Narayanan [1994] also showed that as the iron content of the alloy increased, the number of β-Al_5FeSi phase particles does not increase appreciably, but their size did. Thus, when the iron content was above 0.7 wt%, the β-Al_5FeSi phase tended to crystallize as

extremely large platelets. Although the β-Al_5FeSi phase continues to crystallize until the end of the silicon eutectic reaction, the length of the primary β-Al_5FeSi phase needles greatly depends on the time interval between the β-Al_5FeSi phase start temperature and the silicon eutectic temperature. For this reason, the formation of Fe-rich intermetallic phases and the length of the β-Al_5FeSi phase plates are strongly influenced by the cooling rate.

Otte et al. [1999] and Turmezey et al. [1990] illustrated that high cooling rates, such as experienced in diecasting, reduced the size and amount of β-Al_5FeSi phases in the solidified structure. In addition, high cooling rates also favour the formation of α-$Al_{15}(FeMn)_3Si_2$ phase over β-Al_5FeSi phase. Liu et al. [1999] and Dash and Makhlouf [2001] reported that π-$Al_8Mg_3FeSi_6$ phase is formed by the transformation of β-Al_5FeSi phase. A too high cooling rate, therefore, makes it difficult to transform the β-Al_5FeSi phase into π-$Al_8Mg_3FeSi_6$ phase.

2.3.1 Effects of Fe-rich phases on mechanical properties

It is well known that a high iron content is responsible for inferior mechanical properties in aluminium alloys. This is mainly due to precipitation of β-Al_5FeSi phase. This phase, like most intermetallic particles, is brittle. Its morphology is platelet-like or needle-like (see Figure 2.15), and can be several millimetres long. These two characteristics together decrease the strength and ductility of the cast products [Backerud et al. 1990, Crepeau 1995, Ravi et al. 2002]. Besides impairing mechanical properties, the Fe-rich phases also reduce machinability of castings because of the presence of hard spots [Shabestari et al. 2002].

Archer and Kempf [1931], in their studies on sand cast Al-7Si-0.35Mg alloy, found that the general effect of increasing the iron content from 0.1 to 0.9 wt% was to decrease the tensile strength, and particularly elongation, and to increase slightly the yield strength and Brinell hardness. Their research was supported by many authors who also reported that increasing Fe in aluminium alloys resulted in a drastic reduction in ductility [Grand 1964, Sinfield et al. 1975]. The experimental results of Ravi et al. [2002] confirmed the

role of iron in Al-7Si-0.3Mg alloy, that the Yield Strength (YS), Ultimate Tensile Strength (UTS) and percentage elongation decreased with an increase in Fe content, (from 0.2 to 0.6 wt%), whereas the hardness increased with the Fe content. These results are shown in Figure 2.17.

Horng et al. [2000] investigated the fracture behaviour of A356 alloys by varying the Fe-content within the range of 0.14-0.97 wt%, and their results indicated that when the Fe-content was below 0.57 wt%, the Fe-rich intermetallic phases were mainly π-$Al_8FeMg_3Si_6$ and α-$Al_{15}Fe_3Si_2$ phases, and there was no obvious difference in the fracture resistance. However, with an increased Fe-content to 0.97 wt%, the fracture resistance decreased due to the formation of β-phase. Fatigue cracks were also found to initiate and grow along the eutectic silicon particles and the Fe-rich intermetallic phase.

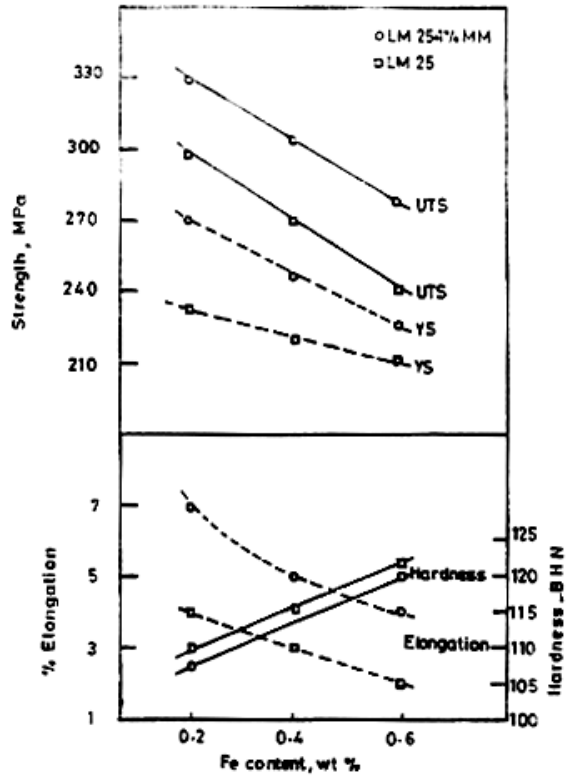

Figure 2.17 The tensile properties of the Al-7Si-0.3Mg alloy contained up to 0.6 wt% Fe [Ravi et al. 2002].

2.3.2 Reduction of effects of Fe-rich phases

Various techniques have been recently demonstrated to minimize the detrimental effect of iron in aluminium alloys. One important method is to add some chemical neutralizers, for example, Mn, Cr, Co, Mo or Ni, to change the morphology from platelet β-Al_5FeSi (a brittle form) to globular or script forms (less brittle forms) [Shabestari et al. 1995, Roy et al. 1996]. However, the addition of a chemical neutralizer, particularly manganese, may result in other problems such as hot tearing or damaging of the furnace wall. The crystallization of a coarse $Al_{15}(FeMn)_3Si_2$ compound, usually termed 'sludge' or 'fall out' in the die casting industry, which has high hardness, a high melting point and high specific gravity compared with the matrix, causes harmful effects, such as hard spot inclusions in castings, causing damage to cutting tools during machining. In addition sludge build up can eventually also reduce the effective capacity of furnaces. Therefore, a high Fe content and the low holding temperature used for die casting alloys makes furnace sludging a significant nuisance [Cao and Campbell 2000, Samuel et al. 2001].

A number of researches demonstrated that a novel method of neutralizing the effect of iron, without any addition of elements such as manganese or chromium, was to superheat the melt to high temperatures before pouring [Narayanan et al. 1994, Crepeau 1995]. As superheat is increased, (up to 500 ^oC above the melting point), the β-phase start temperature decreases until it merges with the silicon eutectic temperature. At this point, the chemical composition of the remaining liquid favours the crystallization of the α-phase. The Chinese script morphology (α-phase) is therefore produced instead of the platelet morphology (β-phase) by a melt temperature of greater than 800 ^oC. However, superheating molten aluminium to such high temperatures is known to increase hydrogen and oxide inclusion contents. Narayanan et al. [1994] also showed that the effect of β-phase could be decreased by increasing cooling rate since this decreased the β-phase growth time and therefore decreased the average length of the β-phase platelets.

On the other hand, iron is not solely a detrimental element. Some beneficial effects of iron do exist, such as increased elevated temperature strength, wear resistance and chip

breaking during machining. Its presence is also necessary in the case of die casting, to prevent the molten alloy from sticking or soldering to the die [Couture 1981].

In summary, the deleterious effects of iron can be decreased by three main techniques; rapid solidification, neutralizer addition and melt superheating. All of these methods basically convert the crystallization of the β-Al_5FeSi phase to the less harmful, Chinese script form.

2.4 Interactions between defects in cast Al-Si-Mg alloys

2.4.1 Interactions between oxide films and porosity

The interactions between oxide film and porosity in cast aluminium alloys have been shown in several researches. Beside the hydrogen content of the melts, it was reported that porosity in aluminium alloy castings was controlled by the initial number of oxide films or, in other words, the cleanliness of the melt [Serratos et al. 2000, Tian et al. 2002]. The cleanliness of melts directly relates with the presence of entrained surface oxide films, submerged into the melt by the action of surface turbulence. Serratos et al. [2000] used a stirring technique to increase the entrained oxide film content. Their results showed that the area of porosity in Al-Si-Mg alloy castings increased with an increase in oxide film content in the melt.

Many authors suggested that oxide films can act as heterogeneous nucleation sites for porosity during solidification due to the presence of porosity associated with oxide films [Eustahopoulos et al. 1985, Kato 1999]. They found that the contact angle between the oxide inclusion and the liquid metal was high (more than 150^o) and might decrease the pressure required for the nucleation of pores. Moreover, the conical cavities occurring in the substrate due to the wrinkled nature of oxide films was thought to be an excellent nucleation site.

Campbell [2003] suggested that double oxide films trapped gas between the two dry sides of films and, once entrained into the melt, acted as pre-existing cavities in the melt. These oxide films could be inflated to become the porosity in the casting. This mechanism is likely to occur in practice meaning that a high pressure is not required for the nucleation stage of the pore. Mi et al. [2003] explained the formation of porosity by entrained oxide film in the following manner. During solidification, the folded oxide film trapped in the melt would be expected to be pushed by the advancing dendritic solidification front. During this time they would unfold to regain their original form as a large planar crack. The driving force for this unfurling would be the gas in solution in the alloy diffusing into the pore. The oxide films, thus, may be responsible for the presence of porosity in castings.

Entrained oxide films can be the most probable sites of both gas porosity and shrinkage porosity in the casting [Campbell 2003]. In cast aluminium alloys with good feeding, oxide films will be inflated and grow only by the rejection of hydrogen from solidified metal while the pressure from shrinkage, combined with hydrogen pressure, will assist the growth of the pore and result in the presence of shrinkage porosity in a casting with poor feeding.

2.4.2 Interactions between oxide films and Fe-rich phases

The interrelationship between oxide films and iron intermetallic compounds in the aluminium alloy castings have been studied and reported that the wetted side of entrained oxide film in cast aluminium alloys is one of the most favourite nucleation sites for Fe-rich phases. The nucleation of platelet β-Al_5FeSi phase on oxide films was proposed by many researchers [Narayanan et al. 1994, Samuel et al. 1998]. Narayanan et al. [1994] used x-ray mapping to investigate the nucleation of Fe-rich phases and x-ray diffraction (XRD) to identify the nature of oxides formed. Their results showed that γ–aluminium oxides are favourable nucleation sites for β-Al_5FeSi phase. They also reported that when the melt was superheated to high temperatures, the γ–aluminium oxide present in the melt transformed to α–aluminium oxide, which was not a good nucleus for the β-Al_5FeSi phase. This led to a decrease in the nucleation potential for the β-phase, observed as a

drop in the β-phase start temperature in the cooling curves with increasing melt superheat. The observation of Simensen and Rolfsen [1997] that π-$Al_8FeMg_3Si_6$ phases formed pre-eutectically on an alumina crucible wall, or on the oxidised melt surface in Al-Si-Mg alloy, also tended to support the concept of its nucleation on oxide.

Cao and Campbell [2001, 2003] studied the precipitation of Fe-rich phase in Al-Si-Mg alloys. They suggested that oxide films were the favourite site for the nucleation of Fe-rich phase and the formation of Fe-rich phases in the cast alloys might not occur without the presence of oxide films. The planar disregistries between some oxides and the α-phase (primary type) were calculated to find suitable matching planes. They reported that MgO, $MgAl_2O_4$, γ-Al_2O_3 and α-Al_2O_3 were good substrates for the nucleation and growth of α-$Al_{15}(FeMn)_3Si_2$ phase. In their work, transverse cracks in the β-Al_5FeSi phases as shown in Figure 2.18 were also observed and they proposed that the fracture of the casting was not caused by the brittleness of Fe-rich phases but the cracks were actually double oxide films which had Fe-rich phases nucleated on their wetted sides. The reduction in the mechanical properties of the casting therefore was due to the interaction between double oxide film and Fe-rich phase.

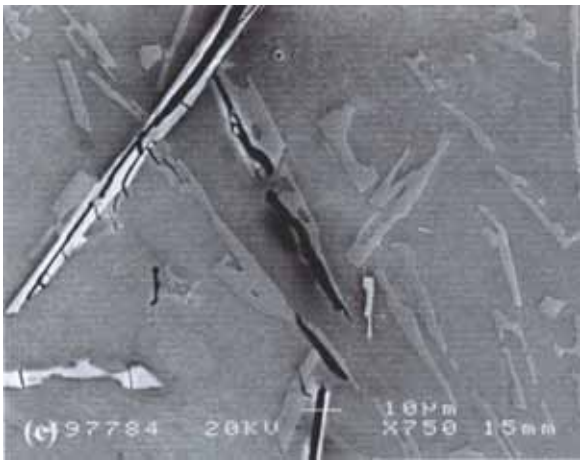

Figure 2.18 The SEM image showing cracks in Fe-rich phases obtained from the cast Al-Si-Mg alloy [Cao and Campbell 2001]

2.4.3 Interactions between Fe-rich phase and porosity

Several researchers reported that porosity formed in association with β-Al_5FeSi phase was usually observed in cast Al-Si-Mg alloys. Villenerve et al. [2001] suggested that increasing the iron content in the cast Al-Si alloys from 0.1 to 1.4 wt% resulted in an increase in porosity, particularly shrinkage porosity, due to the precipitation of long and thick needle (or platelet) of the β-Al_5FeSi phases. These needles are often branched into several needles. Consequently, shrinkage porosity can be formed within the casting due to the inability of the liquid metal to feed into the spaces between these branches.

Roy et al. [1992] claimed that the β-phase platelets served as effective pore nucleation sites. This would influence the amount of porosity that formed in a casting, particularly in a sand mould casting, where the slower cooling rates favoured the formation of β-Al_5FeSi phase.

Otte et al. [1999] stated that the formation of the β-Al_5FeSi phase and the subsequent nucleation of eutectic Si on the β-Al_5FeSi phase may cause a decrease in the permeability of the interdendritic network. This, in turn, could result in reduced feeding with a subsequent increase in porosity and the formation of an extended porosity defect within the casting. The observation of the change in pore morphology in the extended defect, from isolated to more interconnected shrinkage pores, seems to support the consideration that the permeability has been reduced. The experimental results of Otte et al. [1999] revealed that porosity increases with iron content in cast Al-Si-Cu alloy and that with a level of 1.0 wt% Fe 30% more porosity occurred than with 0.1 wt% Fe.

Taylor et al. [1999] studied the formation of porosity in Al-Si alloys and reported that increasing Fe content from 0.4 to 1.0 wt% resulted in a significant increase in the area of porosity and size of porosity. They explained that there were two mechanisms for the deleterious role of iron in porosity formation in aluminium alloys, the restricted feeding theory and the pore nucleation theory. The first theory suggested that the β–Al_5FeSi platelets formed in the interdendritic channels during solidification where they caused a physical restriction to the movement of compensatory feed liquid. Regions undergoing

shrinkage could not be fed adequately and porosity was likely to form as a result. The second theory suggested that β–Al_5FeSi phases were active pore nucleation sites themselves and also physically constrained the growth of the pores and influenced the ultimate pore shape. They further used these mechanisms in the model for predicting porosity in the castings. Their experimental data, however, illustrated that the Fe-rich phases and porosity relationships were somewhat more complex than a simple incremental function based on feeding restrictions by the β–Al_5FeSi phase or pore nucleation upon the β–Al_5FeSi phase since a very high pressure was required for the nucleation of the pore, and a more complex theory was required.

2.5 Statistical analysis of properties of castings

2.5.1 The Weibull distribution

The mechanical properties of cast aluminium alloys normally have a large scatter. There are many statistical tools to describe scattered data, for instance, the Normal or Gaussian distribution (including Log-normal distribution) and various skew-type distributions including the Weibull distribution, Jayatilaka-Trustrum statistics based on Weibull distribution, Type-1 extreme value distribution, Gamma distribution, etc. [Burry 1975].

Statistical distribution models which describe fracture strengths of brittle materials and tensile data are based on the weakest link concept. This simply states that the entire body will fail when the stress at any defect is sufficient for unstable crack propagation. Although there is no universally accepted statistical distribution model which has been used to describe the range of strengths measured in a set of experiments, Green and Campbell [1993] concluded that the Weibull distribution most accurately described the distribution of tensile strength. The Weibull distribution model for description of mechanical properties data of material failed from a single defect distribution has become very popular and well established as a characterisation tool in the field of fracture of engineering materials due to its mathematical simplicity and relatively good success in describing most data.

The Weibull distribution function linearizes most engineering data distributions, making it possible to estimate a population of infinite size from a small amount of data. A Normal distribution is symmetrical about the mean strength, whereas a Weibull distribution is skewed, showing a longer tail of low strengths and a sharper cut-off at high strengths. The behaviour of the data is normally described by a two-parameter function expressed as; [Weibull 1951]

$$F_w = 1 - exp\ \{-(x/\sigma)^{\lambda}\} \tag{2.9}$$

Where F_w is the probability of failures in a tensile test

x is the variable being measured, i.e., tensile strength

σ is a position parameter where 1- 1/e of the samples survive ($\approx$ 37%)

λ is a width parameter, often referred to as the modulus

The value of modulus, λ, can be calculated by taking the logarithm of Equation 2.9 twice over and the linear equation obtained is;

$$\ln\{\ln(1/1\text{-}F_w)\} = \lambda \ln(x) - \lambda \ln(\sigma) \tag{2.10}$$

A straight line can be obtained by plotting $ln\{ln(1/1\text{-}F_w)\}$ versus $ln\ (x)$ with slope λ and intercept $-\lambda ln(\sigma)$. Linear regression analysis is widely employed to evaluate λ. The x values (tensile properties) are arranged in order of increasing value as;

$x_1 \leq x_2 \leq x_3 \ldots \leq x_j \leq x_n$

and a probability of failure will be assigned to each F_w as;

$F_{w,1} \leq F_{w,2} \leq F_{w,3} \ldots \leq F_{w,j} \leq F_{w,n}$

where $0 < F_w < 1$

Because the sample tested is considered representative of a large population the true value of $F_{w,j}$ for each x_j is not known and it has to be estimated. This estimator should be chosen such that, on average, the errors arising each time due to this estimation compensate each other. Several definitions of the probability of failure have been

reported [Khalili and Kromp 1991]. For the j^{th} specimen failure from a total of N results, four of the most common ranking designations are as follows;

$$F_j = \frac{j - 0.5}{N} \tag{2.11}$$

$$F_j = \frac{j}{N+1} \tag{2.12}$$

$$F_j = \frac{j - 0.3}{N + 0.4} \tag{2.13}$$

$$F_j = \frac{j - 0.5}{N + 0.25} \tag{2.14}$$

Khalili and Krompf [1991] investigated these equations using a Monte-Carlo simulation technique and found that the best failure probability estimator was that of equation 2.11.

An example of a skewed distribution, its cumulative plot and an $ln\{ln(1/1\text{-}F_w)\}$ versus $ln(x)$ plot of a theoretical set of UTS data are shown in Figure 2.19. It can be seen that the cumulative distribution is skewed to the right, with a tail of weak specimens extending into the low UTS region. The Weibull plot showed that the fitted line will match the data well (the R value is close to 1), if the tensile property of the specimens is distributed in Weibull manner.

The Weibull distribution is convenient as a tool for casting quality analysis because it enables a single figure quantification (modulus, λ) to be used to describe the strength distribution. This is a more accurate description than a standard deviation, which assumes a symmetrical distribution of strength about a mean value. Generally a minimum of 20 or 30 samples is required for good characterization of the strength of a brittle material [Khalili and Krompt 1991].

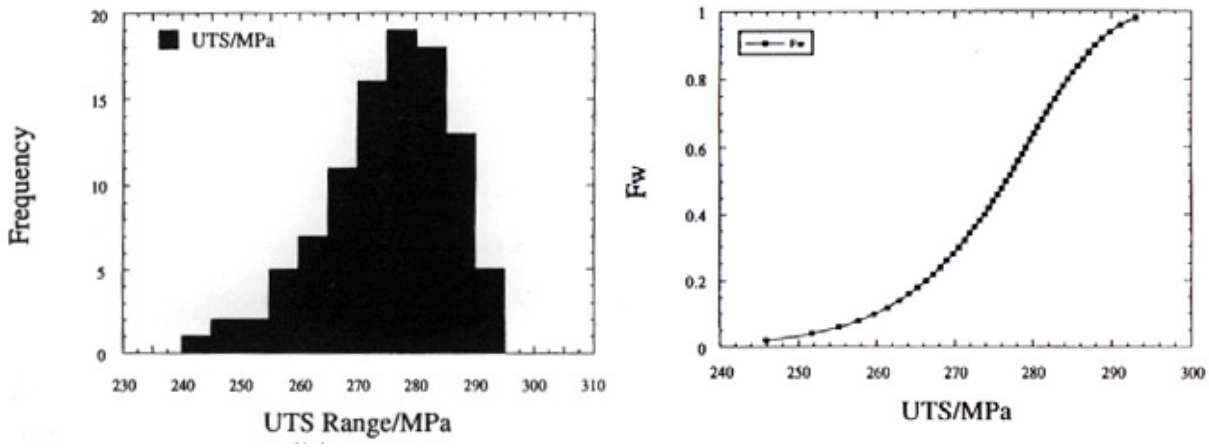

(a) (b)

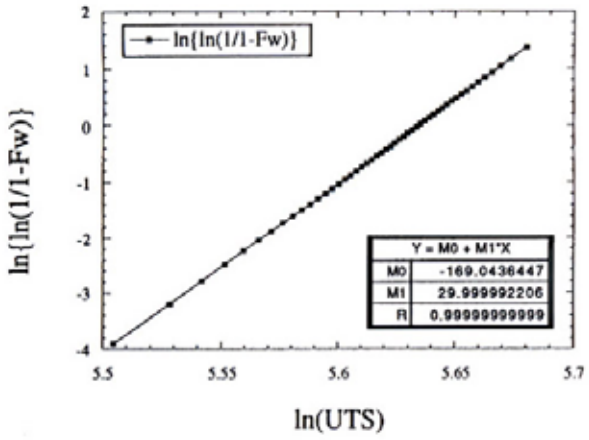

(c)

Figure 2.19 The Weibull distribution showing (a) Frequency, (b) cumulative, and (c) $\ln\{\ln(1/1-F_w)\}$ versus ln (x) plots of a theoretical set of data with modulus λ = 30 and position parameter σ =280 MPa

2.5.2 Yates' algorithm

A very simple technique for estimating the effects and determining the sums of squares in a 2^k factorial design is devised by Yates [Guttman et al. 1982, Montgomery 2000]. To employ the algorithm it is essential that the 2^k experimental combinations must be written down in standard order. Consider the sample data for a 2^3 combination in Table 2.6, i.e; a series of experiments for 3 factors, each of which is varied to two levels. The

column labelled 'Response' contains the corresponding observation (or total of all observations) at the treatment combination. The first half of column (1) is obtained by adding the response by adjacent pairs. The second half of column (1) is obtained by changing the sign of the first entry in each of the pairs in the Response column and adding the adjacent pairs. Column (2) is obtained from column (1) just as column (1) is obtained from the Response column. Column (3) is obtained from column (2) similarly. In general, for a 2^k design we would construct k columns of this type. Column (3) (in general, column (k)) is the contrast for the effect designated at the beginning of the row. To obtain the estimate of the effect, we divide the entries in column (3) by 2^{k-1} (in the example, $2^{k-1} = 4$). Finally, the sums of squares for the effects are obtained by squaring the entries in column (3) and dividing by 2^k.

Table 2.6 Yate's Algorithm for sample data

Combination	Response	(1)	(2)	(3)	Effect	Estimate of Effect (3)/ 2^{k-1}
(1)	-4	-3	1	16	I	-
a	1	4	15	24	A	6.00
b	-1	2	11	18	B	4.50
ab	5	13	13	6	AB	1.50
c	-1	5	7	14	C	3.50
Ac	3	6	11	2	AC	0.50
bc	2	4	1	4	BC	1.00
abc	11	9	5	4	ABC	1.00

2.6 Summary

The quality of cast aluminium alloys is affected by several microstructural defects with Fe-rich intermetallic phases being one of the most detrimental defects in aluminium castings. The presence of Fe-rich phases, particularly the brittle β-Al_5FeSi platelet, results in a dramatic decrease in mechanical properties, especially ductility and tensile strength of the alloys. The deleterious effects can be decreased by decreasing the size of

the Fe-rich phases or changing their form to one less harmful. Porosity is another major defect in the castings. The most frequently found porosity in cast aluminium alloys are gas porosity and shrinkage porosity. The formation of porosity, therefore, directly relates to the hydrogen content in the melt and shrinkage during solidification. However, their nucleation mechanisms have been discussed by many authors because the pressures required for both homogeneous and heterogeneous nucleation are very high and the possible mechanisms for porosity formation still need to be established. This porosity causes loss of tensile properties because it may act as discontinuities in the structure, stress concentrators, and initiation sites for cracks. Oxide film defects are the most recently discovered defects that have been of more and more interest as it has become apparent that folded oxide films can act as cracks in the casting. In addition, oxide films are difficult to detect by non-destructive testing methods. Oxide films, therefore, make the mechanical properties of aluminium alloys both uncontrollable and unpredictable.

Microstructural defects not only have direct effects on mechanical properties but many researchers have shown that these defects are usually found together and seem to have relationships between them. However, there is no research that can clearly explain their interactions. To know the formation and characteristics of each microstructural defect and their interactions will help the development of quality control techniques, and improve mechanical properties of aluminium alloy castings. The present research, therefore, is an attempt to investigate the relative magnitudes of the major types of defect, with respect to mechanical properties. In addition, the nucleation of the various defects, Fe-rich phases, hydrogen porosity and their association with oxide film inclusions is also studied.

CHAPTER 3

EXPERIMENTAL PROCEDURE

This study was aimed at investigating the three most important defects that have been identified as influencing the properties of cast aluminium alloys, namely, oxide films, Fe-rich phases and porosity (hydrogen gas porosity and shrinkage porosity). The objective was to examine the effects of these microstructural defects, and their interrelationships, on tensile properties. Therefore the experimental work was split into four parts. The first experiment was carried out to investigate the effects of Fe-rich phases, hydrogen porosity, oxide films, and their interactions, on the tensile properties in an Al-Si-Mg alloy. The second experiment was carried out to investigate the effects of oxide films and shrinkage porosity on the tensile properties of the Al-Si-Mg alloy, with different Fe contents. A third experiment was carried out to investigate the effects of oxide films on the formation of hydrogen porosity in high purity aluminium and a high purity Al-7 wt% Si alloy. Finally, a fourth experiment was carried out to investigate any interrelationship between oxide films and shrinkage porosity in the Al-Si-Mg alloy. The details of each experiment are described in the following.

3.1 Interactions between Fe-rich phase, hydrogen porosity and oxide film in Al-Si-Mg alloy.

In order to study the effect of the three microstructural defects and their interactions, an experiment was carried out where each of the three defects was introduced at a different level, low and high. The experiment therefore contained 8 combinations of detrimental factors. All experimental combinations were cast in the test bar moulds shown in Figure 3.1, and the bars subjected to tensile testing to observe how their mechanical properties varied. Details of the 8 experiments are shown in Table 3.1. The fracture surfaces of the test bars, and a microstructural sample taken from the test bar and the runner bar, were also examined to investigate their microstructures and determine the presence of microstructural defects in the casting.

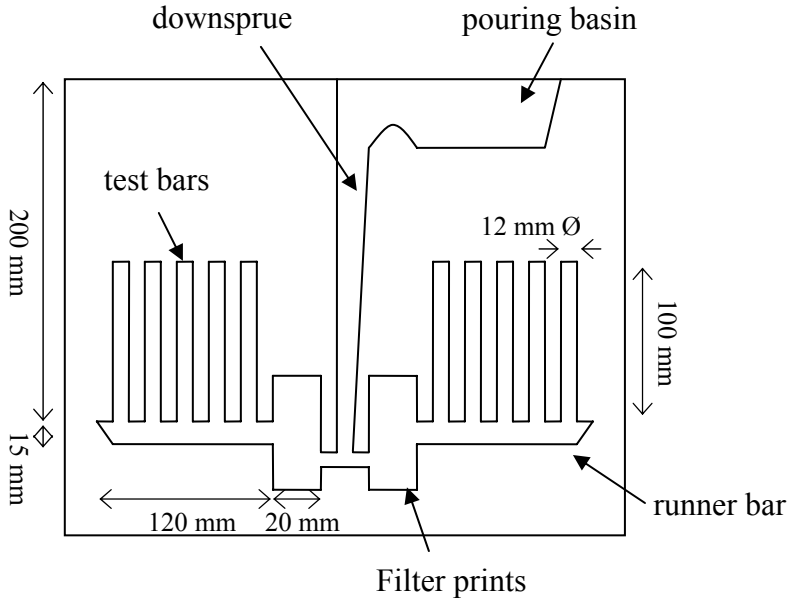

Figure 3.1 Dimensions of the tensile test bar mould

Table 3.1 Details of the 8 combinations of experimental work.

Experiment	1	2	3	4	5	6	7	8
Fe content (wt %)	low (0.1)	high (0.5)	low (0.1)	high (0.5)	low (0.1)	high (0.5)	low (0.1)	high (0.5)
Hydrogen content	low (0.1 ml/100g)		high (0.45 ml/100g)		low (0.1 ml/100g)		high (0.45 ml/100g)	
Oxide film content	low (Filtered casting)				high (Unfiltered casting)			

3.1.1 Materials and sample preparation

The alloy used in this experiment was a 2L99 alloy with a specific chemical composition of 7.3 wt% Si, 0.3 wt% Mg and 0.1 wt% Fe. The alloy was divided into 2 types, a low and high Fe content, that contained 0.1 wt% and 0.5 wt% of Fe respectively. To prepare the high Fe alloy, an Al-20 wt% Fe masteralloy was prepared separately in an induction furnace and added into the 2L99 molten alloy in order to increase the Fe content. The

samples from the melts were analyzed using glow discharge spectrometry to determine their chemical compositions and Table 3.2 shows the actual chemical compositions obtained from the low and high Fe content melts. The results show that the low Fe content experimental alloy contained 0.10 wt% Fe, 7.01 wt% Si and 0.35 wt% Mg, while the high Fe content experimental alloy contained 0.49 wt% Fe, 6.95 wt% Si and 0.33 wt% Mg.

Table 3.2 Chemical compositions of the low and high Fe content Al-Si-Mg alloys.

	Composition (% wt)									
	Si	Mg	Fe	Mn	Cu	Ni	Zn	Sn	Ti	Al
Low Fe casting	7.01	0.35	0.10	<0.005	0.01	0.014	<0.015	<0.005	0.15	Balance
High Fe casting	6.95	0.33	0.49	<0.005	0.01	0.016	<0.015	0.031	0.15	Balance

The molten alloy was further divided into 2 types by making a change in hydrogen content. A rotary fluxing and degassing machine was used to remove hydrogen gas from the molten alloy to obtain a low hydrogen content (rotor speed 400 rpm, flux feed rate 20 g/min. and injection time 4 minutes). In order to increase the hydrogen content, 400 g of Hydral40, (a proprietary addition used for increasing the hydrogen content of aluminium die casting alloys), was added to the molten alloy. The hydrogen gas measurement instrument used in this experiment was an AlScan, a nitrogen gas recycling probe. The hydrogen content measured in the low hydrogen content castings was 0.11 ml/100g metal, as planned, while 0.45 ml/100g metal was obtained in the high hydrogen content castings.

The pattern used for this experiment was the tensile test bar mould shown in Figure 3.1. Each mould contained ten test bars, each with a diameter of 12 mm and length of 100 mm. The runner bar had a cross section of 15 mm deep and 20 mm wide. To produce 2 different contents of oxide films, (low and high), the cast moulds were divided into 2 types as follows; the first type, (the low oxide film content), contained 20 ppi (20 pores

per linear inch) ceramic filters of dimensions 50x50x20 mm, placed in the filter prints at the entrance of the runner bar from the sprue. For the test bars with a high oxide film content, the filter print was retained but no filter was inserted. The ceramic foam filter is thought to remove previously formed inclusions, and also reduce the speed of flow of the molten alloy filling the mould in order to prevent any further oxide film from being entrained. Removing the filters meant that oxide films already present were not removed and more oxide films were introduced by surface turbulence in the empty filter print. The running systems were examined using a real-time x-ray machine to assess the extent of surface turbulence and the extent to which the surface oxide film was probably entrained.

Figures 3.2a to 3.2f show x-ray images obtained from a filtered mould; the low oxide film content casting. It can be seen that the flow of molten alloy in the filtered mould was smooth and produced no noticeable surface turbulence. This suggested that few entrained oxide films would be introduced into the casting during the filling process. The x-ray images obtained from an unfiltered mould (the high oxide film content casting) have been shown in Figures 3.3a to 3.3f. These images show that the surface turbulence associated with the flow was greater than in the filtered mould and therefore that oxide films introduced into the liquid metal would be greater. In addition, the surface turbulence in the unfiltered mould also leads to entrained air bubbles as shown in Figures 3.3e and 3.3f.

The aluminium alloy used for each experimental combination was prepared in a resistance heated melting furnace and the casting temperature was 730 ^{o}C. Once the correct melt composition was achieved, the alloy was carefully poured into a mould, which had already been placed in a roll-over device. Immediately after pouring was completed the mould was gently rotated through 180^{o} and left for about 5 minutes, to ensure directional solidification of the casting towards the runner bars, which would now be acting as feeders, and hence solidification shrinkage in the test bars was avoided. Three moulds were poured in each case, giving 30 test bars, for each combination of factors.

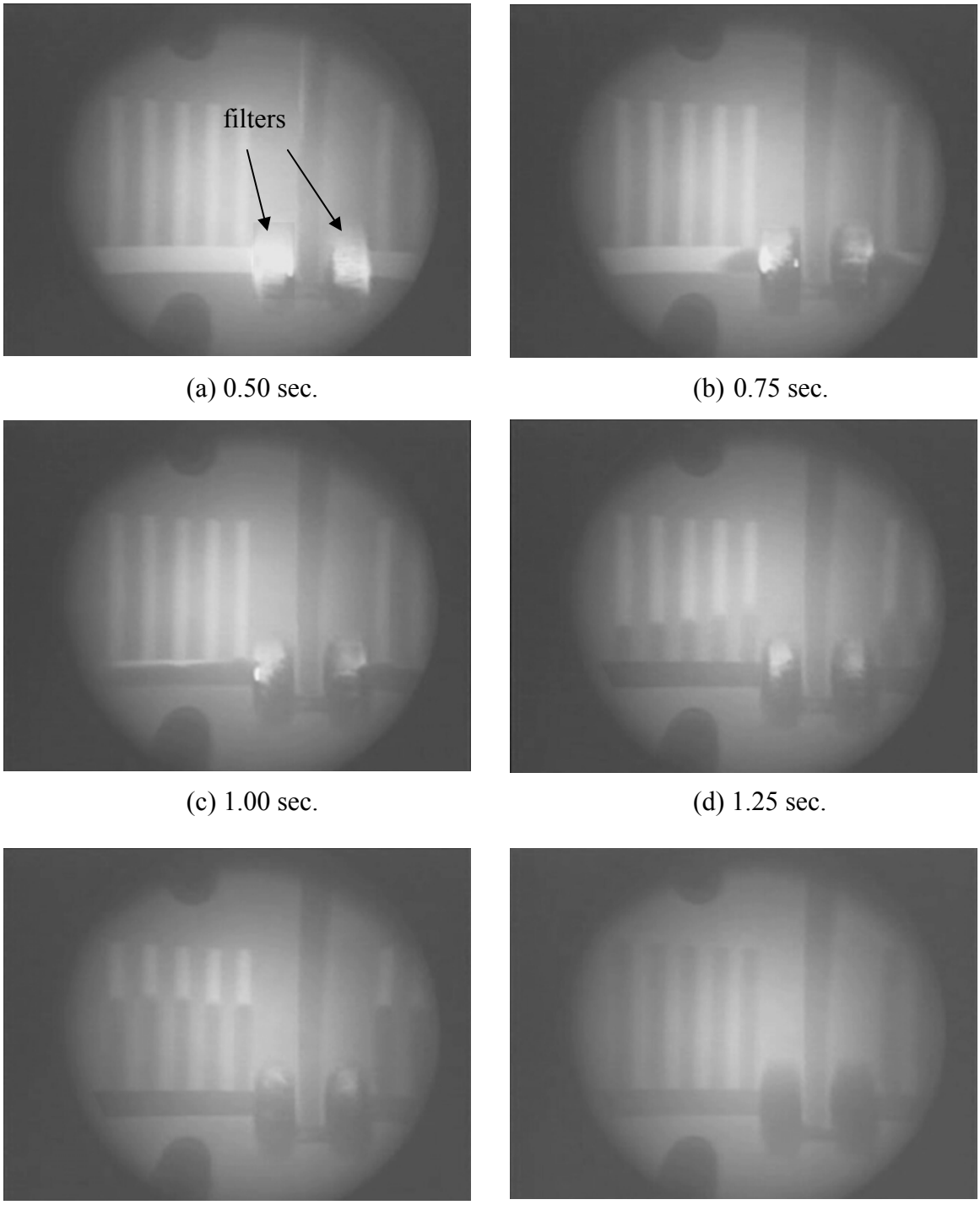

(a) 0.50 sec. (b) 0.75 sec.

(c) 1.00 sec. (d) 1.25 sec.

(e) 1.50 sec. (f) 2.00 sec.

Figure 3.2 X-ray images showing the flow of liquid metal in the filtered mould.

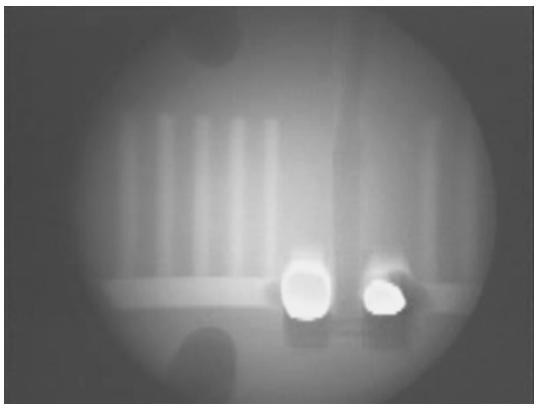

(a) 0.75 sec.

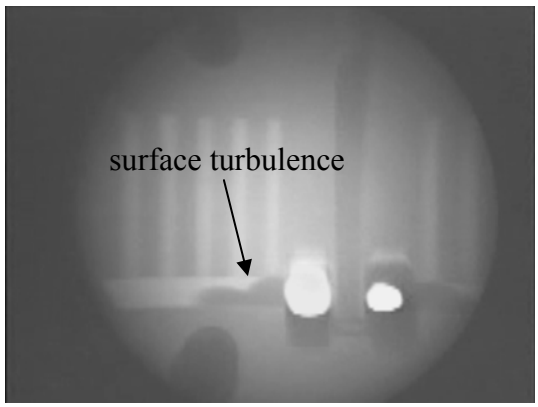

(b) 0.87 sec.

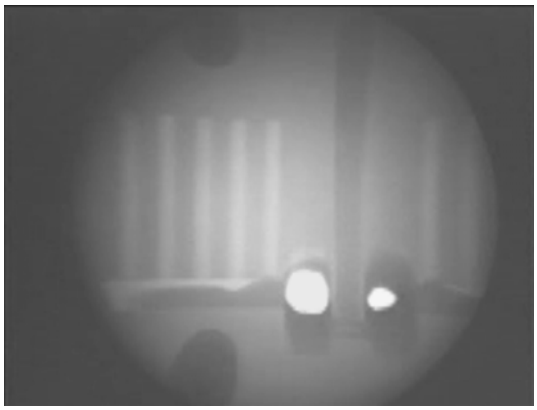

(c) 1.00 sec.

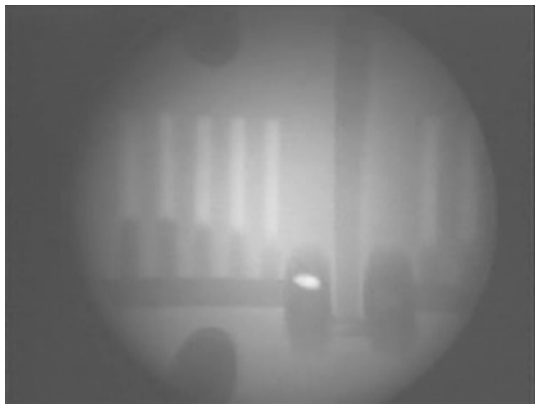

(d) 1.25 sec.

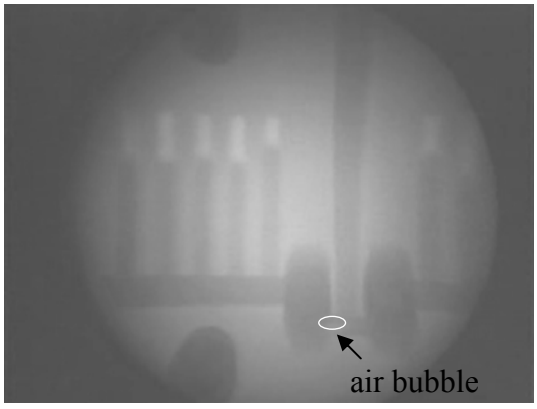

(e) 1.50 sec.

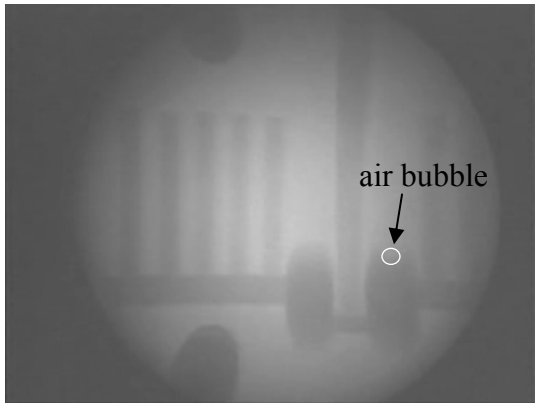

(f) 2 sec.

Figure 3.3 X-ray images showing the flow of liquid metal in the unfiltered mould.

In this experiment, a PREFIL Footprinter was used to assess the cleanliness of the molten alloy before casting. This measures the flow rate of a 1400 gram sample of a melt, pressurized through a filter. Comparisons of the gradients of weight versus time graphs provided a relative measure of cleanliness. The results of the melt filtration tests for the low Fe content alloy and the high Fe content alloy have been shown in Figure 3.4. This results demonstrated that the act of increasing the Fe content of the alloy resulted in only a slight reduction in the cleanliness of the liquid metal used in the experiments. Therefore, the entrained oxide films produced in the low and high oxide film content experiments were varied significantly as a result of the use of the different running systems only.

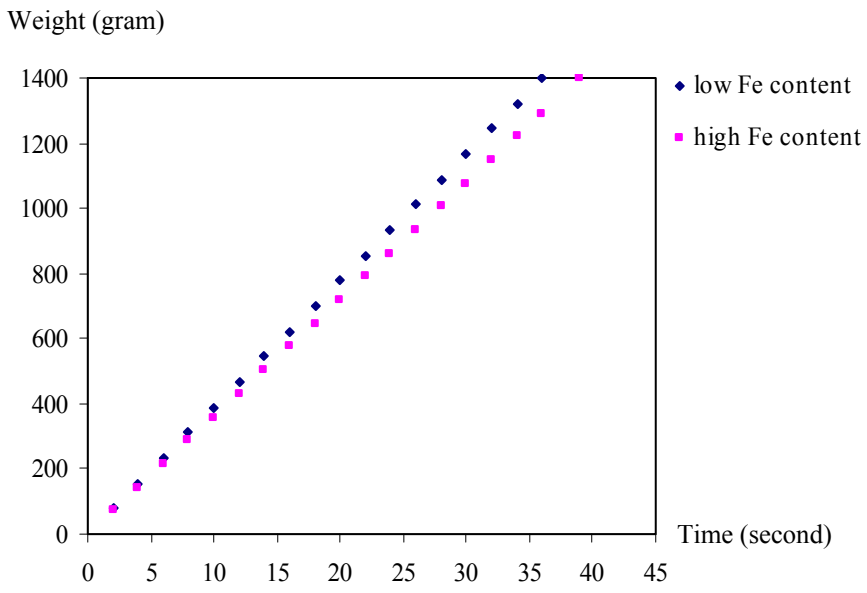

Figure 3.4 Graph of filtration weight versus time, showing the cleanliness of the liquid metal.

After cooling, the cast test bars were solution treated at 540 ^{o}C for 17 hours in an air circulating furnace, and then quenched in hot water (at 80 ^{o}C). They were subsequently held at -20 ^{o}C and precipitation treated at 160 ^{o}C for 5 hours. The heat treated specimens were machined according to British Standard (BS EN 10002-1: 2002) [BSI 2001], to obtain dimensions of 6.75 mm diameter and 25 mm gauge length on a 40 mm parallel

length. Tensile testing was carried out with a screw-driven Zwick testing machine with a cross-head speed of 1 mm/min, equivalent to a strain rate of $4x10^{-4}$ s^{-1}. The elongation of the sample was measured from the load-displacement curves derived from the cross head movement of the machine.

3.1.2 Metallographic examination and image analysis

Samples for metallographic examination were cut from test bars and the runner bar from each experiment, mounted in a conducting resin, ground on 120, 240, 400, 800 and 1200 grit SiC paper respectively, and polished with 6, 1, and 0.25 μm diamond pastes on cloth. The polishing was completed using magnesia powder to produce a mirror-like finish. The polished specimens were examined using a LEICA optical microscope and a Phillips XL30 scanning electron microscope (SEM). Energy dispersive x-ray (EDX) analysis was used to determine the compositions of particles found within the samples. The fracture surfaces of some typical tensile specimens, particularly those from the low Ultimate Tensile Strength specimens, were also examined using scanning electron microscopy (SEM) in order to investigate microstructural defects on the fracture surfaces.

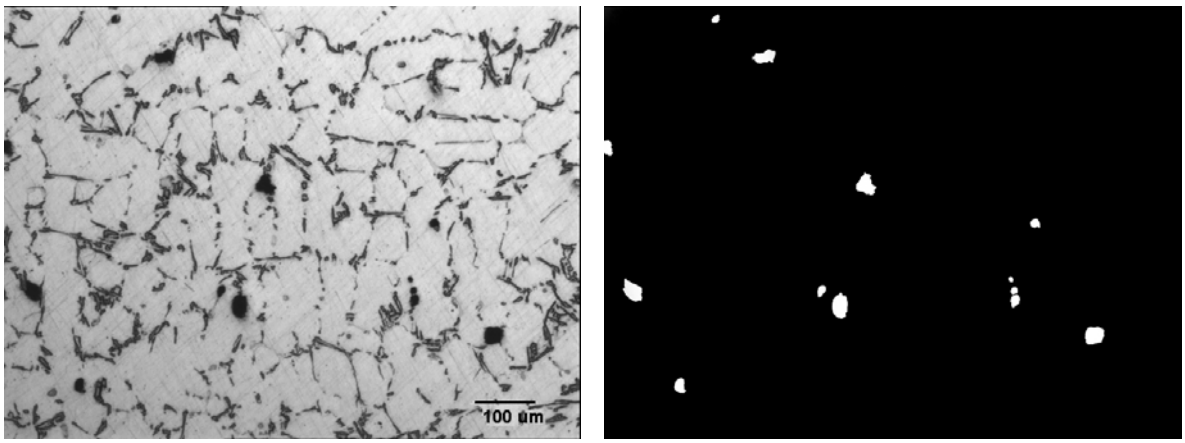

(a) (b)

Figure 3.5 (a) an optical micrograph taken for image analysis obtained from the cross-section of the runner bar (b) an image of pores in the microstructure obtained from computer software.

Micrographs of the polished specimens obtained from the runner bar of each experimental combination were taken with a magnification of x50 and adjusted by Photoshop software in order to detect porosity defects in the microstructure as shown in Figure 3.5. A hundred images of each experimental combination were subjected to image analysis using KS 400/3.0 software to calculate area of porosity, number of pores per cm^2 and mean pore size.

3.2 Interactions between Oxide film and shrinkage porosity in a low and high Fe content Al-Si-Mg alloy.

This experiment was carried out to study the effects of entrained oxide films, shrinkage porosity and their interaction, on the tensile properties of cast Al-Si-Mg alloy. Two Fe contents were used. Both oxide film and shrinkage porosity were divided into 2 levels, therefore, there were 4 combinations of detrimental factors for each alloy. Details of the 4 experimental combinations are shown in Table 3.3.

Table 3.3 Details of the 4 combinations of experimental work.

Experiment	1	2	3	4
Oxide film content	low (filtered)	high (unfiltered)	low (filtered)	high (unfiltered)
Shrinkage porosity	low (180^o rotated mould)		high (no-rotation of the mould)	

3.2.1 Materials and sample preparation

The 2L99 alloy used in the low Fe content experiment had the chemical composition of 0.08 wt% Fe, 6.92 wt% Si and 0.31 wt% Mg as shown in Table 3.4. The high Fe content experiment alloy, also prepared by adding an Al-20Fe masteralloy, had the chemical

composition of 1.12 wt% Fe, 6.90 wt% Si and 0.23 wt% Mg. It can be seen that the Mg content in the low and high Fe content alloy was different by about 0.1 %, which might influence the tensile properties of the castings, precluding any direct comparison between the results of the two experiments. Therefore the experiment became that of 2 separate groups of castings (an Al-7Si-0.3Mg-0.1Fe alloy and Al-7Si-0.2Mg-1.1Fe alloy).

The aluminium alloy was charged into a resistance heated melting furnace and heated to 730 ^{o}C. A rotary fluxing and degassing machine was used to remove hydrogen gas, as well as inclusions, from the molten alloy, (rotor speed 400 rpm, flux feed rate 20 g/min. and injection time 4 minutes). The hydrogen contents, measured by an AlScan, were 0.18 ml/100g metal in the low Fe content castings and 0.20 ml/100g metal in the high Fe content castings. In other words both groups of castings had comparable hydrogen gas levels.

Table 3.4 Chemical compositions of the low Fe content and the high Fe content Al-Si-Mg alloys.

	Composition (% wt)									
	Si	Mg	Fe	Mn	Cu	Ni	Zn	Sn	Ti	Al
Low Fe casting	6.92	0.31	0.08	<0.005	<0.005	0.006	<0.005	0.13	0.14	Balance
High Fe casting	6.90	0.23	1.12	0.026	0.012	<0.005	<0.015	0.12	0.12	Balance

The pattern used for this experiment was the same pattern used in the previous experiment, (see Figure 3.1), and to produce different contents of oxide films, the cast moulds were divided into 2 types, with low and high oxide film content. The first type contained 20 ppi ceramic filters placed in the filter prints and in the second type, the filter print was retained but no filter was inserted. Moreover the runner bar was increased in size to 30 mm deep and 20 mm wide in order to produce greater surface turbulence of the molten alloy while filling the mould. Figures 3.6a to 3.6h show the flow of molten alloy in the unfiltered mould with the increased runner bar size. This showed that surface

turbulence was produced and ensured the presence of more entrained oxide films than in the first experiment (see Figures 3.2a to 3.2f and 3.3a to 3.3f).

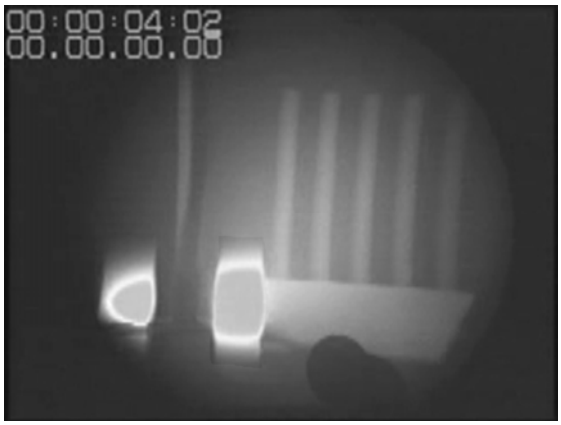

(a) 0.25 sec.

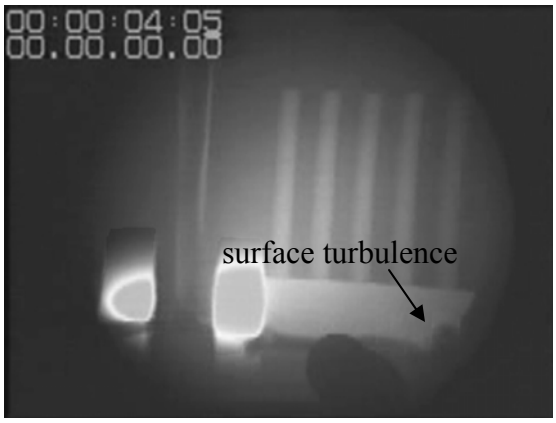

(b) 0.375 sec.

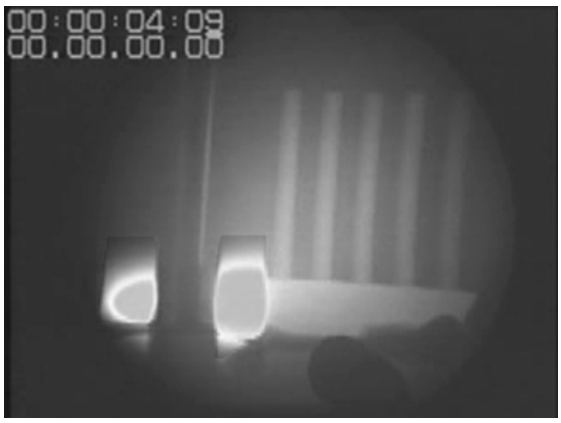

(c) 0.5 sec.

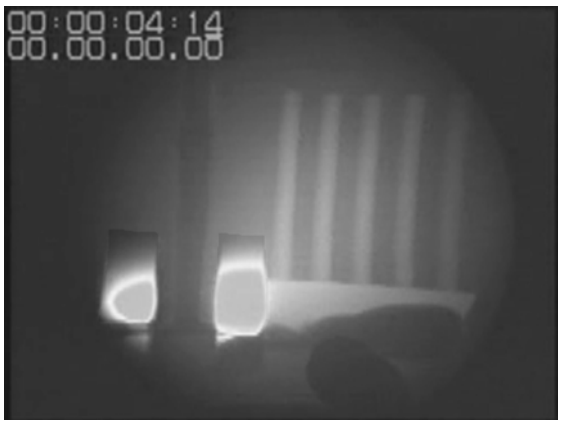

(d) 0.75 sec.

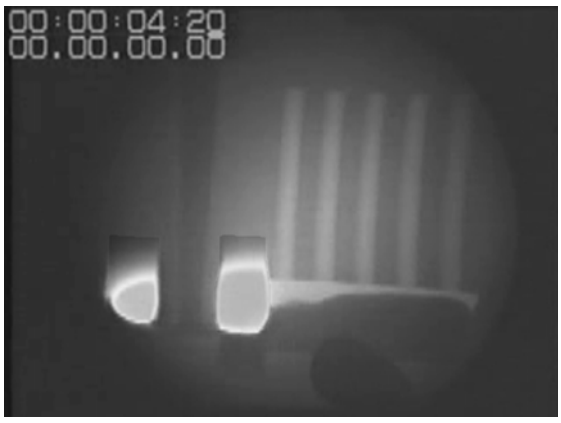

(e) 1.0 sec.

(f) 1.5 sec.

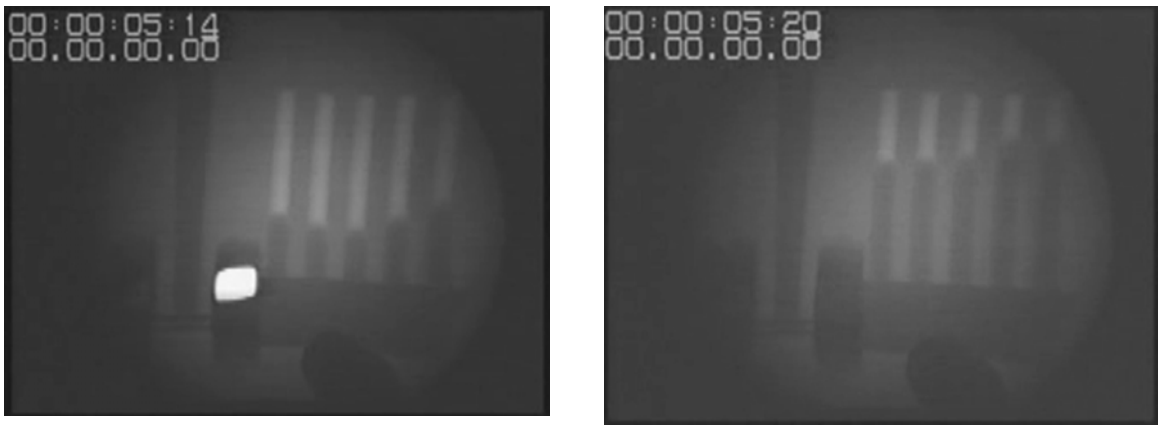

(g) 1.75 sec. (h) 2.0 sec.

Figure 3.6 X-ray images showing flow of liquid metal obtained from high oxide film casting.

Differences in amount of shrinkage porosity were obtained by using the mould rotation technique. The low shrinkage porosity mould was placed in a roll-over device and after pouring was completed the mould was rotated through 180^{o} and left for about 5 minutes to ensure directional solidification of the casting towards the feeder and minimise shrinkage in the test bars. For the casting with higher shrinkage porosity, the mould was not rotated after filling. As in the previous experiment, three moulds were poured in each case, giving 30 test bars for each experimental combination. Again the cleanliness of the starting molten alloy was examined by the PREFIL Footprinter. Figure 3.7 shows the results obtained from the low Fe content and the high Fe content experiment. The molten alloy in the low Fe content castings was slightly cleaner than the high Fe content castings since the pressurizing time for the 1400 gram melt in the case of the low Fe content castings was 31 seconds compared to 33 seconds in the case of the high Fe content castings. However the cleanliness of both experiments was essentially comparable. After the castings were heat treated and machined to obtain the standard dimensions as explained in section 3.1. Tensile testing was carried out as before to investigate the effect of oxide films and shrinkage porosity on the tensile properties of the castings.

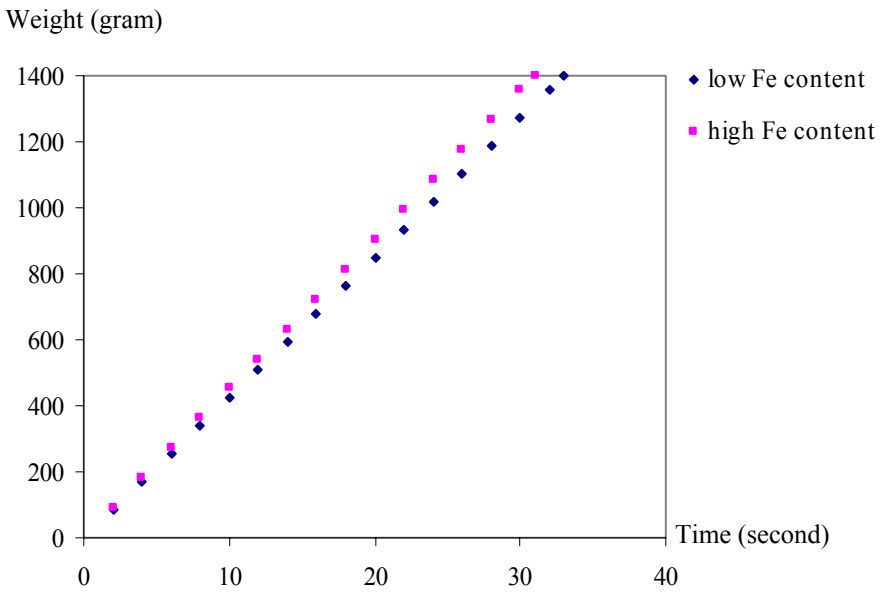

Figure 3.7 Graph of filtration weight versus time, showing the cleanliness of the liquid metal.

3.2.2 Metallographic examination and image analysis

Samples for metallographic examination were cut from the test bars and the runner bars of the castings. Some fracture surfaces, particularly those from the low tensile property test bars, were subjected to examination of their fracture surfaces and image analysis was carried out on samples from the runner bar of each of the experimental combination castings. The procedures for preparing the samples and the image analysis method were as for the previous experiment (see section 3.1.2).

3.3 Effects of entrained oxide films on the formation of hydrogen porosity in high purity aluminium and a high purity Al-Si alloy

This experiment was carried out to investigate the effects of entrained oxide films on the formation of hydrogen porosity specifically in high purity aluminium and a high purity Al-Si alloy. Again low and high contents of oxide films were prepared in each

experimental alloy, and the castings was made with the same conditions as in the previous experiments; therefore, their characteristics could be compared to the other experiments.

3.3.1 Materials and sample preparation

The materials used in this experiment were high purity aluminium (99.99 wt% Al) and high purity silicon (99 wt% Si). To prepare the high purity Al-7 wt% Si alloy, the high purity aluminium was melted in an induction furnace and the high purity silicon added. The actual chemical compositions of the melts produced have been shown in Table 3.4. This shows that the Al-Si alloy had 7.02 wt% Si, as planned, while the Fe contents in the pure aluminium and Al-Si alloy were 0.03 and 0.05 wt% respectively, (i.e., below or close to the solubility of Fe in Al, as planned).

Table 3.4 Chemical compositions of the pure aluminium and Al-7 wt% Si alloy

	Composition (% wt)									
	Si	Mg	Fe	Mn	Cu	Ni	Zn	Sn	Ti	Al
Pure Al	ND.	<0.19	0.03	0.02	0.01	<0.005	<0.015	0.08	0.03	balance
Al-7Si	7.02	<0.19	0.05	0.02	0.01	<0.005	<0.015	0.08	0.03	balance

The mould used in this experiment was the tensile test bar mould used in the previous experiments, (see Figure 3.1). In order to introduce different contents of oxide films the moulds were again divided into 2 types, the first type contained ceramic filters in the filter prints at the entrance of the runner bar whereas in the second type of mould filters were not inserted. A mass of 3 kg of each experimental alloy was melted in an induction furnace and heated to 730 ^{o}C for casting in each mould. To increase the hydrogen content in the molten alloy, 100 grams of Hydral40 were added. The hydrogen content in the high purity aluminium castings was 0.41 ml/100g metal, and in the high purity Al-Si

alloy castings was 0.38 ml/100g metal. One unfiltered mould was cast from each alloy and the moulds were rotated through 180 ^{o}C to avoid solidification shrinkage in the test bars.

3.2.2 Metallographic examination and image analysis

Samples for metallographic examination were cut from the test bar and the runner bars of the castings of each experimental combination. Micrographs obtained from each experimental combination were subjected to image analysis to calculate porosity area, number of pores per cm^2 and the mean pore size. The procedures for preparing the samples, and image analysis methods, were the same as in the previous experiment (see section 3.1.2).

3.4 Effects of entrained oxide films on the formation of shrinkage porosity in Al-Si-Mg alloy.

In order to study the effects produced by entrained oxide film defects on the formation of shrinkage porosity, the mould used was changed to a plate mould that introduced both types of defect in the castings. Figure 3.8 shows the running system and dimensions of the mould used in the experiment. The plate had dimensions of 200x100x15 mm and the runner had dimensions of 15 mm deep and 15 mm wide.

Modelling software (MAGMAsoft) was used to study the flow of the molten alloy, and the temperature changes during the solidification process, to ensure that entrained oxide films and shrinkage porosity were produced in the castings. Figures 3.9a to 3.9f show the results of computer modelling of the flow of the molten aluminium alloy during filling of the plate mould using no filter, and no stopper in the pouring basin. Figures 3.10a to 3.10d show the temperature distribution of the alloy in the mould after pouring was completed.

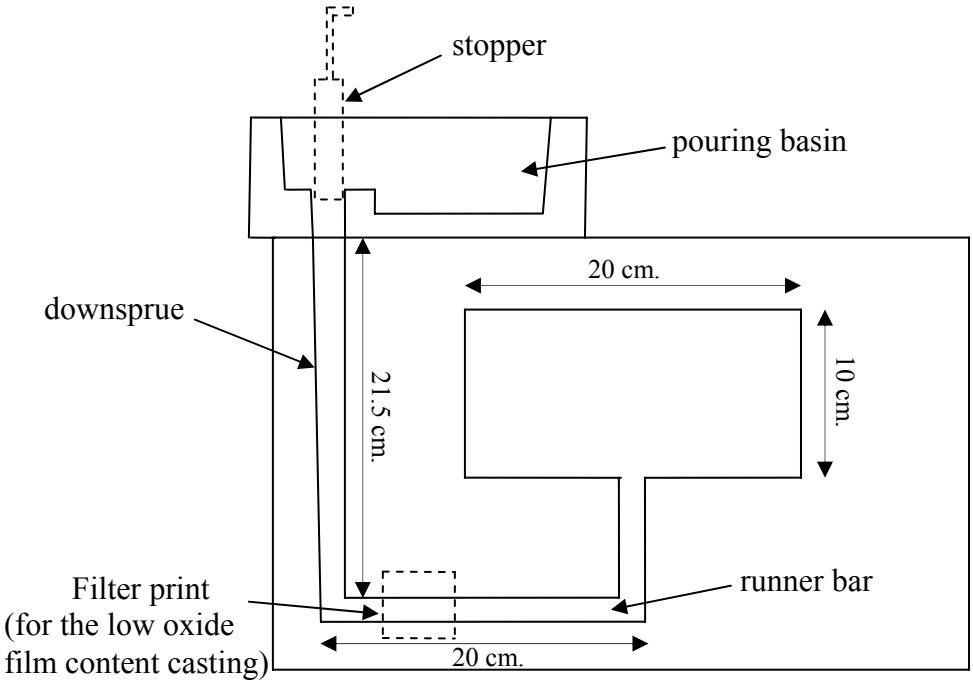

Figure 3.8 Dimensions of the plate mould used in the experiment.

The images obtained from the computer model show that surface turbulent flow of the liquid alloy was produced in the plate mould and numbers of oxide films would be entrained in the casting during the filling process. It can be seen in the results of the temperature modelling that the casting started to solidify at the edges of the plate and that the centre of the plate was the last zone to solidify. Shrinkage porosity, therefore, was likely to be formed in this area.

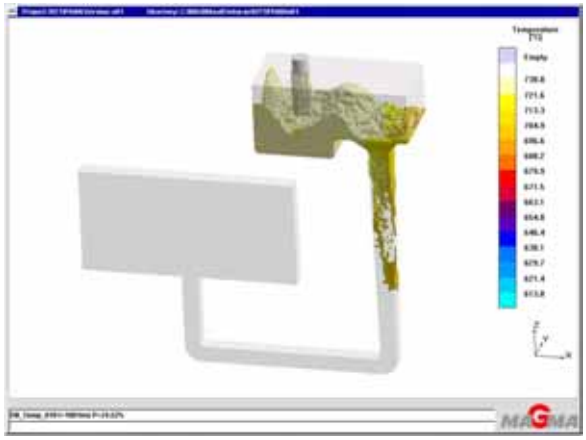

(a) 1.0 sec.

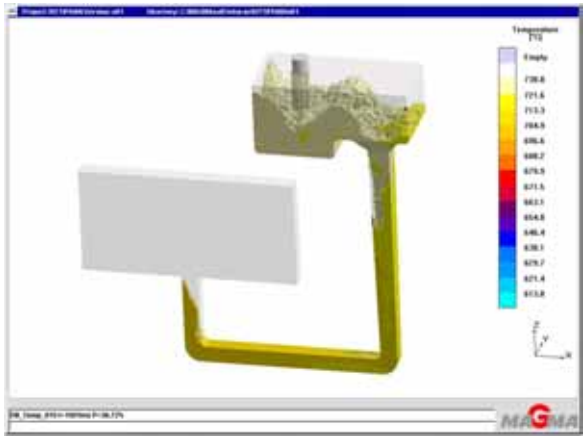

(b) 1.5 sec.

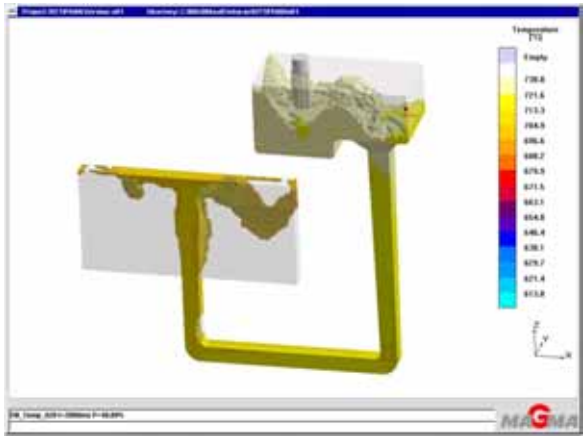

(c) 2.0 sec.

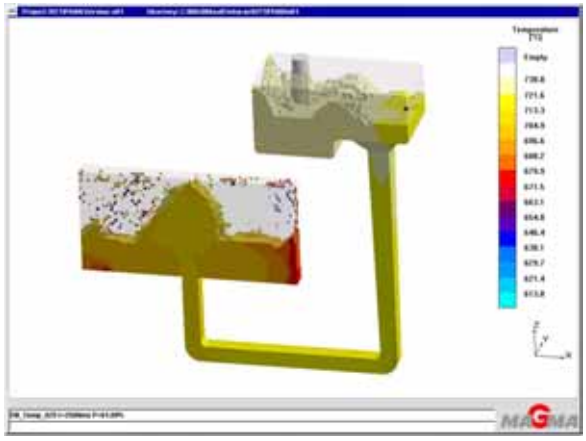

(d) 2.5 sec.

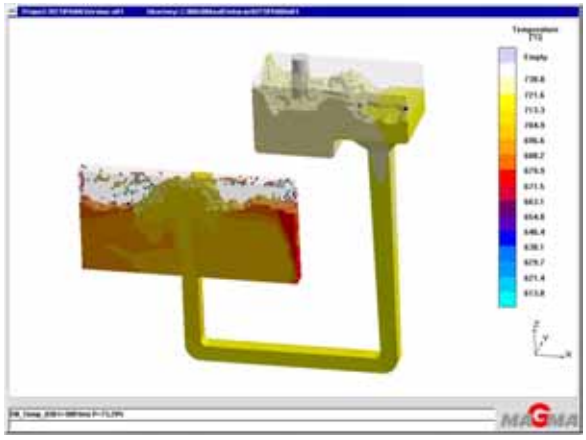

(e) 3.0 sec.

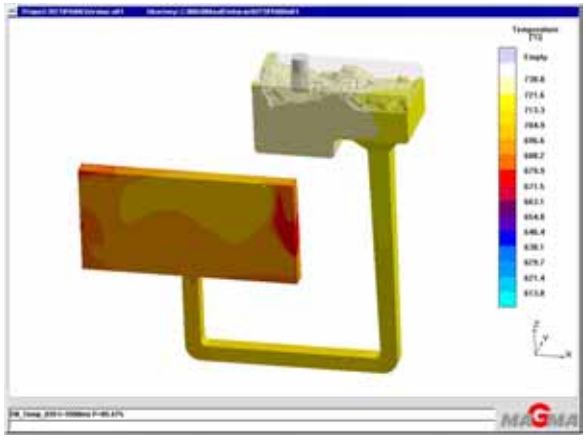

(f) 3.5 sec.

Figure 3.9 Images of the flow of liquid aluminium alloy in the unfiltered mould obtained from the modeling software.

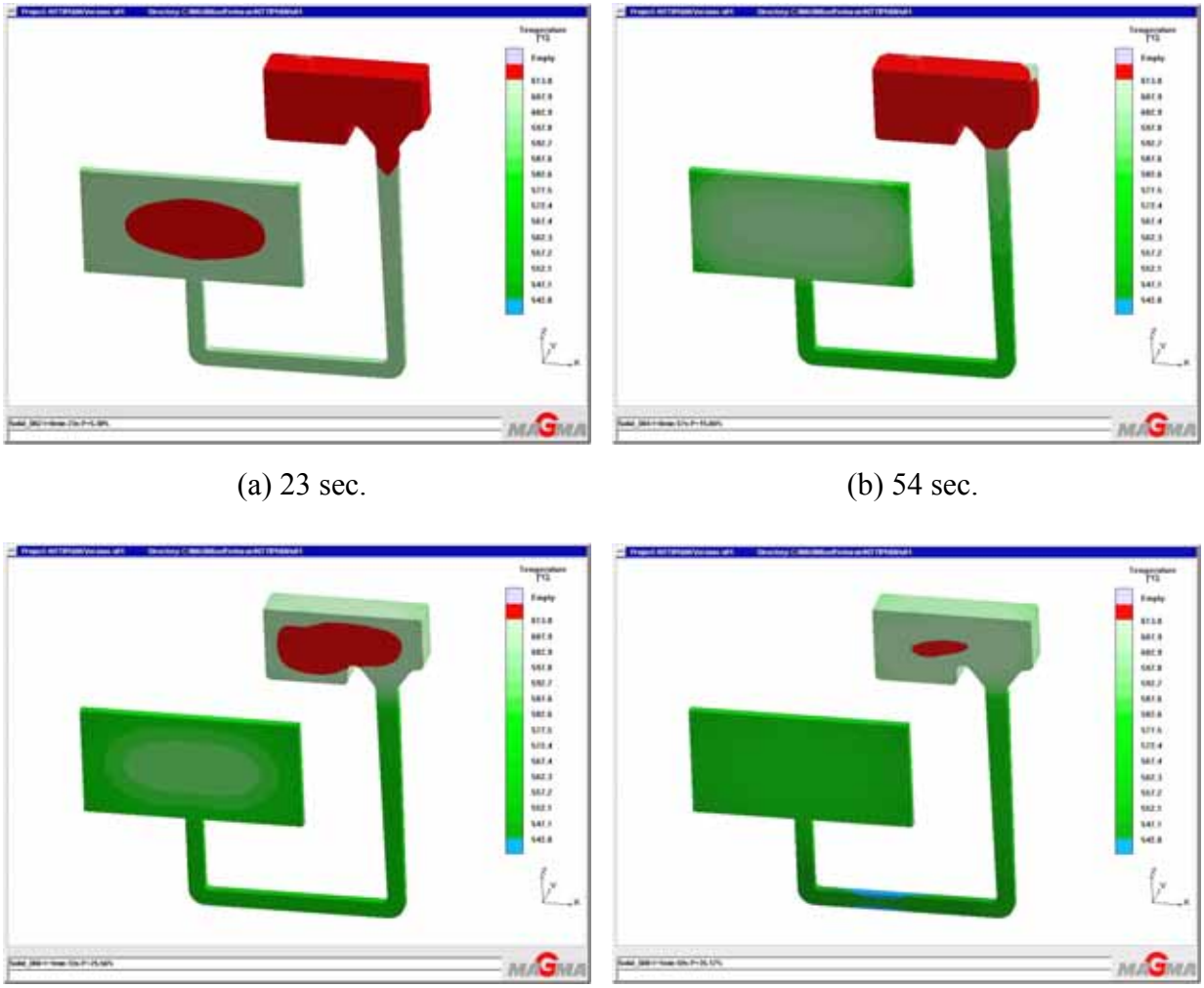

(a) 23 sec. (b) 54 sec.

(c) 1 min 33 sec. (d) 1 min 59 sec.

Figure 3.10 Image of temperature change in the solidification process of the aluminium alloy obtained from the modelling software.

3.4.1 Materials and sample preparation

In this experiment, the 2L99 alloy used had the chemical composition of 6.98 wt% Si, 0.35 wt% Mg and 0.10 wt% Fe as shown in Table 3.5.

Table 3.5 Chemical composition of the Al-Si-Mg alloy used in the experiment to determine the formation of shrinkage porosity.

Alloy	Composition (% wt)									
	Si	Mg	Fe	Mn	Cu	Ni	Zn	Sn	Ti	Al
2L99	6.98	0.35	0.10	0.002	<0.001	<0.001	0.015	<0.001	0.144	Balance

A mass of 3 kg of the alloy was melted in an induction furnace and heated to 730 ^{o}C. One plate mould was cast in the case of each oxide film content. The plate moulds were classified into 3 types, to produce different contents of oxide films as follows: the first type contained a 20 ppi ceramic filter placed in the filter print at the entrance of the runner from the sprue. The second type was a normal plate mould as shown in Figure 3.8 (i.e., cast without a filter) and finally, the third type was the normal plate mould but a stopper was used and removed when the molten alloy filled up the pouring basin. In addition, stirring the melts with a flat paddle attached to a rotary drilling gun operated at about 200 rpm for 2 minutes was done before casting this mould. The purpose of stirring was to introduce oxide films into the melt. The running systems of each mould type were examined using a real-time x-ray machine to assess the likely entrainment of the surface oxide film.

Figures 3.11a to 3.11f show x-ray images obtained from a filtered mould. This shows that the filter placed in the mould reduced the speed of the liquid metal flow resulting in quiescent flow, showing that few entrained oxide films would be introduced into the casting during the filling process. Figures 3.12a to 3.12e show real-time x-ray images of the flow obtained from the unfiltered and unstoppered mould. Surface turbulence was produced, although it was less than that predicted by the modelling software, (Figures 3.9a to 3.9f), however the images demonstrated that the oxide films introduced into the casting would be greater than in the filtered casting.

(a) 0.5 sec.

(b) 1.0 sec.

(c) 1.5 sec.

(d) 2.5 sec.

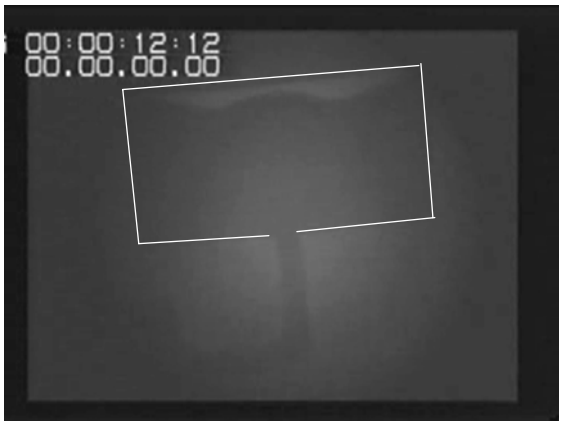

(g) 3.5 sec.

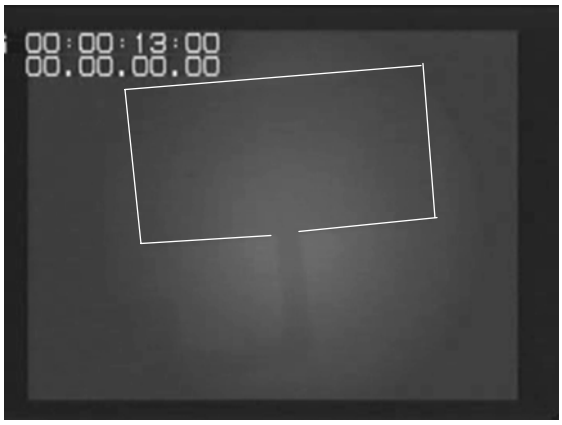

(h) 4.0 sec.

Figure 3.11 Real-time x-ray images showing the flow of liquid metal in the filtered mould.

(a) 1.0 sec.

(b) 2.0 sec.

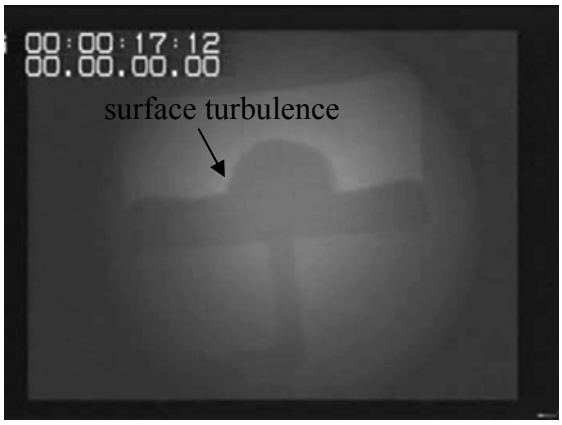

(c) 2.5 sec.

(d) 3.0 sec.

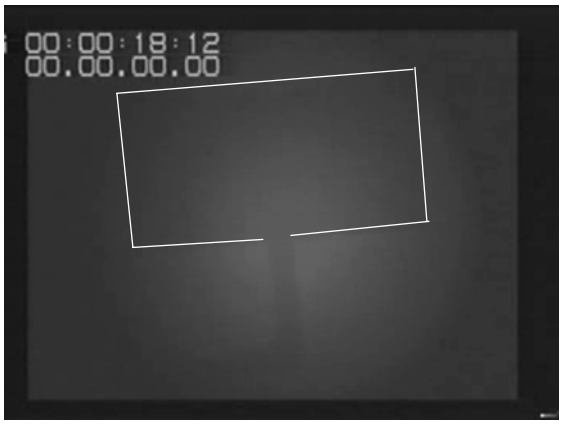

(e) 3.5 sec.

Figure 3.12 Real-time x-ray images showing the flow of liquid metal in the unfiltered and unstoppered mould.

(a) 0.50 sec.

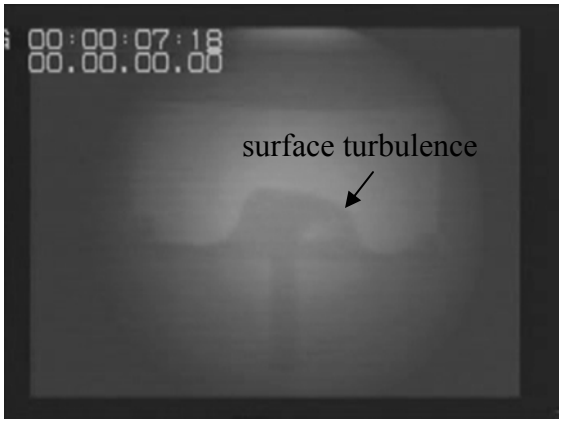

(b) 0.75 sec.

(c) 1.0 sec.

(d) 1.25 sec.

(e) 1. 5 sec.

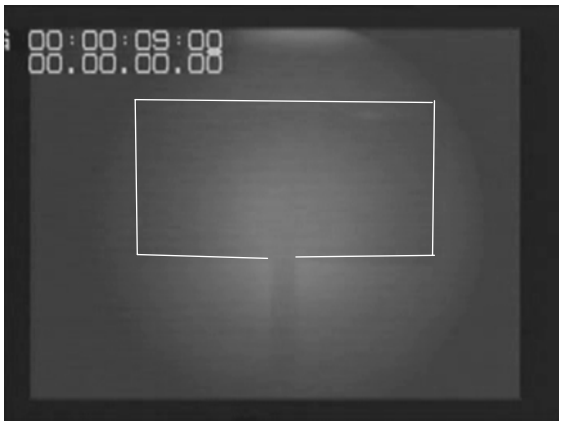

(f) 2.0 sec.

Figure 3.13 Real-time x-ray images showing the flow of liquid metal in an unfiltered and stoppered mould.

Figures 3.13a to 3.13f show the real-time x-ray images of the flow obtained from the unfiltered and stoppered mould. Surprisingly, there was much surface turbulence produced in the filling process, despite the use of a stopper, a commonly-used tool for reducing oxide film defects in the casting. The stopper was placed in the sprue entrance and raised when the basin was filled to the correct level. This would allow only clean metal to enter the sprue and improve the filling of the sprue to create a smooth flow of liquid metal and minimize its surface turbulence [Campbell 2004]. However, it was demonstrated that the use of a stopper increased the fill time by 60 percent [Latimer and Read 1976]. This suggestion was supported by the real-time x-ray images since the fill time used in the unfiltered and stoppered mould was about 2 seconds while the fill time of unstoppered mould (Figure 3.12) was about 3.5 seconds. This showed that stopper influence the velocity of liquid metal flow and the high velocity of flow resulted in an increase in the splash and surface turbulence of liquid metal, particularly in the bad running system as this experiment. This, therefore, suggests that the greatest amount of entrained oxide films introduced into the unfiltered and stoppered casting compared to the other moulds.

The x-ray images, therefore, indicated that the three types of mould used in this experiment produced different entrained oxide film contents, from low to high in the order of filtered mould, the unfiltered and unstoppered mould, and the unfiltered and stoppered (using stirred alloy) mould respectively.

The hydrogen gas measurement technique used in this experiment was the LECO method. The solid samples of each oxide film content castings required for this method were cast in a LECO sample die. The hydrogen content measured for the filtered casting was 0.20 and for the unfiltered and unstopperred casting was 0.21 ppm. However, the hydrogen content in the unfiltered and stoppered casting (the high oxide film casting) increased to about 0.34 ppm due to the stirring of the melt.

3.4.2 Density measurement

Density measurement is one of the methods used to examine the amount of porosity in a casting and the casting quality can be related to the density of the sample. The cast plates

were cut equally into 32 sections, (of dimensions 25 mm high and 25 mm wide), defined in numerical order from left to right and from top to bottom as shown in Figure 3.14. Each sample was weighed in air and in water and calculated the density. The density of each section was calculated according to Archimedes' Principle, where the apparent weight of an object immersed in a liquid decreased by an amount equal to the weight of the volume of the liquid that it displaced. The difference between the two masses (in air and in water) would show the density of the section as the following equation shows:

$$D = \frac{d \times Mass_{in\ air}}{Mass_{in\ air} - Mass_{in\ water}} \qquad (3.1)$$

where *D* is the density of the section and *d* is the density of water (1 kg/m^3)

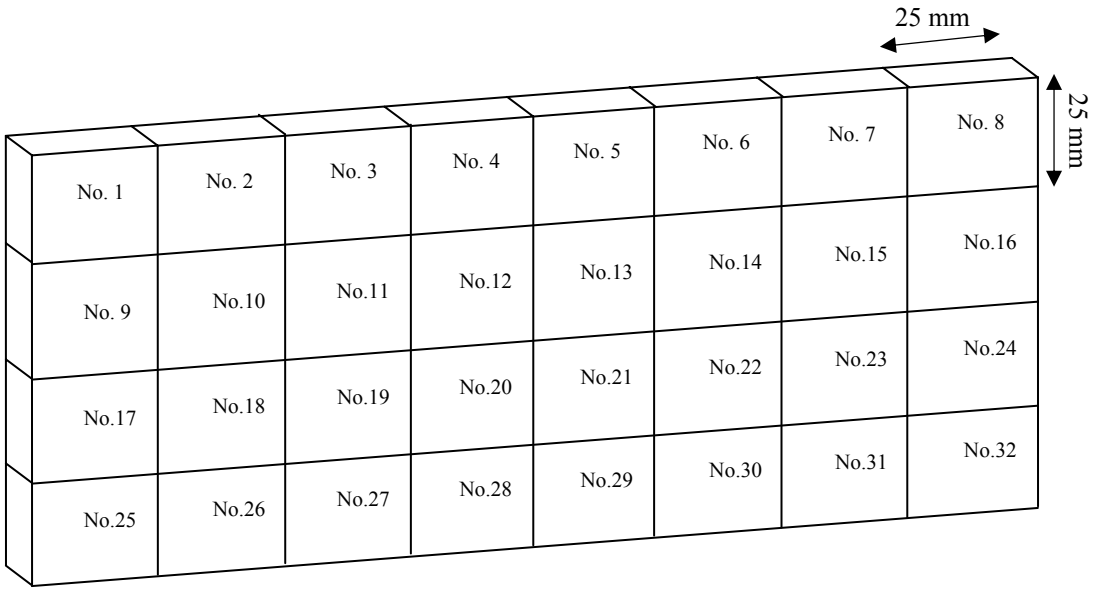

Figure 3.14 The 32 sections of the cast plate used for density measurement and image analysis.

3.4.3 Metallographic examination and image analysis

Each sample was also analysed using image analysis. The 32 samples obtained from the cast plates were cut along their midplane and ground on 120, 240, 400, 800 and 1200 grit SiC paper. Images of all cross sections were digitized with a resolution of 600 pixels per inch by the scanner and subjected to image analysis using Sigma Plot Scan Pro 5 software to calculate the area of porosity, number of pores and mean length of pore. Examples of the scanned image, and the image obtained from image analysis, have been shown in Figure 3.15.

The selected sections were further polished and their microstructures examined. The procedures for preparing the samples were the same as in the previous experiments (see section 3.1.2).

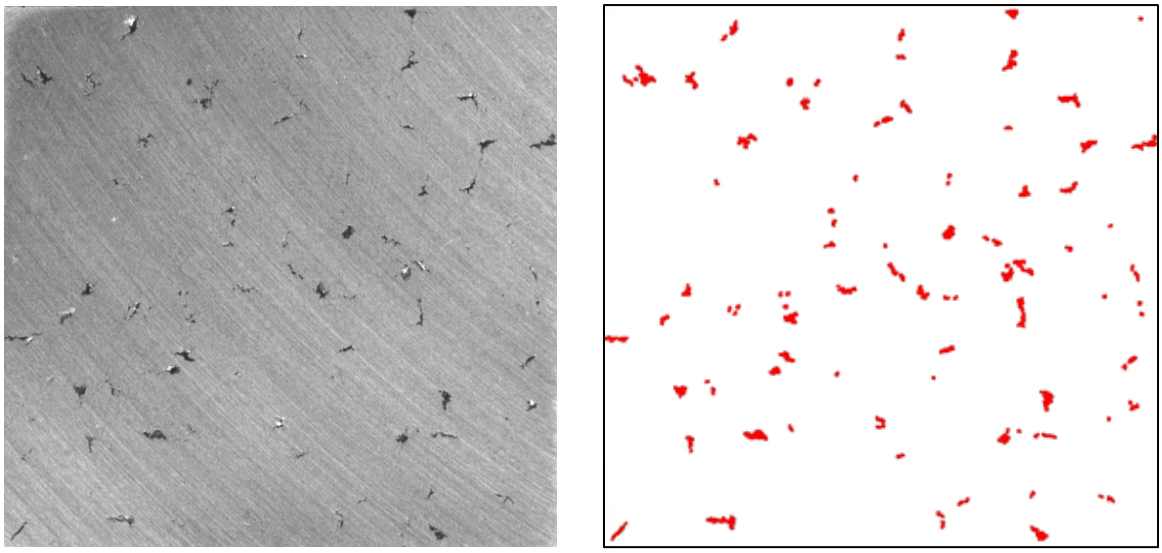

Figure 3.15 (a) The optical micrograph taken for the image analysis (b) an image of pores in the castings obtained from the image analysis software.